ResearchGate

See discussions, stats, and author profiles for this publication at:
https://www.researchgate.net/publication/304341121

Ion microprobe 208Th–208Pb ages from high common Pb monazite, Morefield Mine, Amelia County, Virginia…

Article *in* American Journal of Science · May 2016

DOI: 10.2475/05.2016.03

CITATIONS
0

READS
174

2 authors:

Elizabeth J. Catlos
University of Texas at Austin
83 PUBLICATIONS **2,241** CITATIONS

SEE PROFILE

Nathan R. Miller
University of Texas at Austin
42 PUBLICATIONS **403** CITATIONS

SEE PROFILE

Some of the authors of this publication are also working on these related projects:

Project
Tectonometamorphic history of the central Menderes Massif, western Turkey
View project

Project
U-PB AGE OF THE OLDEST AIR-BREATHING LAND ANIMAL View project

All content following this page was uploaded by Elizabeth J. Catlos on 24 June 2016.

The user has requested enhancement of the downloaded file. All in-text references underlined in blue are added to the original docu
and are linked to publications on ResearchGate, letting you access and read them immediately.

[American Journal of Science, Vol. 316, May, 2016, P. 470–503, DOI 10.2475/05.2016.03]

ION MICROPROBE ^{208}Th-^{208}Pb AGES FROM HIGH COMMON Pb MONAZITE, MOREFIELD MINE, AMELIA COUNTY, VIRGINIA: IMPLICATIONS FOR ALLEGHANIAN TECTONICS

ELIZABETH J. CATLOS† and NATHAN R. MILLER

The University of Texas at Austin, Jackson School of Geosciences, Department of Geological Sciences, 1 University Station C9000, EPS 1.130, Austin, Texas 78712

ABSTRACT. Monazite [(Ce,Th)PO_4] from a pegmatite in the Morefield Mine of the eastern Piedmont of central Virginia has unusually high and variable amounts of common Pb, leading to problematic interpretations of its U-Th-Pb ages and how the monazite relates to nearby granite intrusions and faults. To address these issues, we analyze a single large monazite grain from the pegmatite using electron microprobe analysis (EMPA, n = 64), laser ablation-inductively coupled plasma mass spectrometry (LA-ICP-MS, n = 58), and secondary ion mass spectrometry (SIMS, n = 59). The monazite study grain exhibits compositional variations in proximity to microcracks consistent regions of secondary alteration and recrystallization. Although the compositions of these regions fit the ideal stoichiometry of monazite, they have lower Si, Th, U, and Y, and higher P, rare earth element (REE), and Ca concentrations compared to visibly unaltered portions of the grain. LA-ICP-MS and SIMS analyses demonstrate that common Pb, as proxied by ^{204}Pb, is enriched in proximity to microcrack regions and correlates with ^{137}Ba. SIMS ^{232}Th-^{208}Pb analysis from grain regions with lowest contents of common Pb (^{208}Pb comprises >99% of Pb isotopes) yields two sets of ages: 263.5±3.0 Ma (±1σ; MSWD = 1.7; n = 11) and 234.1±3.3 Ma (±1σ; MSWD = 0.4; n = 13). Regionally, the ages are similar to the youngest Appalachian pegmatite bodies emplaced during the terminal (Alleghanian) Laurentia-Africa collision. However, the monazite ages are younger than locally surrounding intrusions. The closest intrusive in distance (~30 km) and age is the Petersburg granite (296.33±0.11 Ma, zircon ^{238}U-^{206}Pb), the emplacement of which coincided with activity along the Hylas Fault. Because the fault experienced a brittle-ductile transition in the Late Permian (~262 Ma), coeval with the older ^{232}Th-^{208}Pb monazite age group, we postulate that the Hylas Fault may have operated as a fluid migration system between the Petersburg granite and Morefield Mine pegmatite. The younger monazite age coincides with Triassic normal and/or sinistral faulting linked to the development and deformation of local rift basins.

Keywords: monazite, geochronology, Amelia monazite, Morefield Mine pegmatite, Appalachians Piedmont

INTRODUCTION

Monazite [(Ce,Th)PO_4] from the Morefield Mine granitic pegmatite district of Amelia County, Virginia (fig. 1) is known for high common Pb contents, as measured by laser ablation inductively coupled plasma mass spectrometry (LA-ICP-MS) and thermal ionization mass spectrometry (TIMS; Peterman and others, 2006; Kohn and Vervoort, 2008; Peterman and others, 2012). The problem of obtaining reproducible and reliable ages from the Morefield Mine pegmatite monazite (also the "Amelia" or "Smithsonian" monazite, Peterman and others, 2006; Kohn and Vervoort, 2008; Peterman and others, 2012) has complicated understanding the tectonic evolution of the eastern Piedmont of central Virginia. The pegmatite body intrudes an enigmatic suite of granulite-facies rocks, termed the Goochland Terrane (fig. 1), that itself has a debated origin and tectonic evolution (Glover and others, 1983; Farrar, 1984; Rankin and others, 1989; Smerekanicz and Dudas, 1999; Bailey, 2004; Bailey and Owens, 2012). How emplacement of the pegmatite relates to granitic intrusions in the region

† Corresponding author: ejcatlos@gmail.com

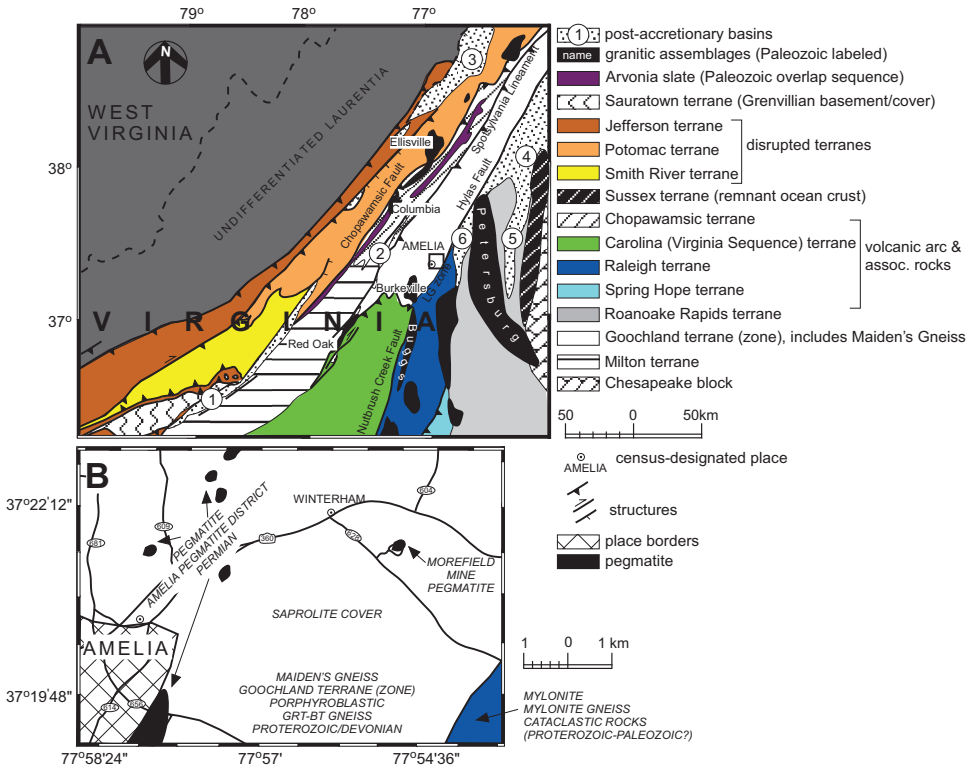

Fig. 1. (A) Schematic geological map after VDMR (2003) with location of Raleigh Terrane after Hibbard and others (2002). Basins are numbered: 1: Dan River-Danville Basin, 2: Cumberland, 3: Culpepper, 4: Taylorsville, 5: Petersburg-Studley; 6: Richmond. Box indicates region in panel B. (B) Regional geological map of the Morefield Mine and Amelia Pegmatite District using geological information from Dicken and others (2008). Exposure is poor and up to 20m of saprolite cover bedrock (Smerekanicz and Dudas, 1999). LG zone = Lake Gordon mylonite zone.

also remains unclear (Farrar, 1984). The present study provides important new information regarding the age, paragenesis, and chemical evolution of the Amelia monazite, which prospectively constrains the evolution of the pegmatite within the tectonic history of the central Appalachians.

Monazite is thought to exclude common Pb during crystallization (Corfu, 1988; Parrish, 1990; Seydoux-Guillaume and others, 2002), in theory making the mineral ideal for U-Th-Pb geochronological methods and applications. This assumption is vital for dating monazite by electron microprobe analysis (EPMA), which cannot discriminate against a common Pb component (Suzuki and others, 1994; Montel and others, 1996). Compositional analyses of monazite by mass spectrometric methods, however, demonstrates that variable amounts of common Pb can occur (Tilton and Nicolaysen, 1957; Parrish, 1990; Boggs and others, 2002; Catlos and Çemen, 2005; Lobato and others, 2007; Hoisch and others, 2008; Kempe and others, 2008; Kohn and Vervoort, 2008; Krenn and others, 2008a, 2008b; Morelli and others, 2010; Krenn and others, 2011; Li and others, 2011; Aleinikoff and others, 2012; Janots and others, 2012; Peterman and others, 2012; Seydoux-Guillaume and others, 2012). Indeed, inconsistent U-Th-Pb ages previously determined for the Amelia monazite exemplify problems associated with dating accessory phases with high common Pb contents (table 1) (Kohn and Vervoort, 2008; Peterman and others, 2012).

TABLE 1

Ages from the Morefield Mine pegmatite and nearby igneous intrusions[a]

Age (Ma, ±σ)	Method[b]	Reference
	Columbia	
598±80	Rb-Sr whole rock (±1σ)	Fullagar (1971)
459.1±7.3	U-Pb zircon SIMS (±1σ)	Sinha and others (2012)
457±7	U-Pb zircon SIMS (±1σ)	Wilson (ms, 2001)[c]
454±9	Rb-Sr whole rock	Mose and Nagel (1982)
342±70	Rb-Sr whole rock (±1σ)	Fullagar (1971)
	Petersburg	
330±8	U-Pb zircon ID-TIMS (±2σ)	Wright and others (1975)
300.08±0.10	U-Pb zircon (porphyritic) ID-TIMS	Buchwaldt and Owens (2012)[c]
296.33±0.11	U-Pb zircon (medium-grain) ID-TIMS	Buchwaldt and Owens (2012)[c]
	Buggs Island	
313±15	not indicated	Druhan and Rollins (1984)[c]
314±16	Rb-Sr whole rock	Kish and Fullagar (1978)[c]
285±10	not indicated	Druhan and Rollins (1984)[c]
	Red Oak	
354±3	U-Pb zircon	Horton and others (1999)[c]
	Ellisville	
444±6	U-Pb zircon SIMS (±1σ)	Wilson (ms, 2001)[c]
443.7±4.4	U-Pb zircon ID-TIMS (±2σ)	Hughes and others (2013)
441±8	Rb-Sr whole rock	Pavlides and others (1982)
440.9±3.3	U-Pb zircon SIMS (±1σ)	Sinha and others (2012)
438±10	Pb-Pb zircon (±1σ)	Pavlides and others (1994)
436.8±4.2	U-Pb zircon ID-TIMS (±2σ)	Hughes and others (2013)
427.9-344.8	^{40}Ar/^{39}Ar biotite (±1σ)	Pavlides and others (1994)
429.5±2.1	^{40}Ar/^{39}Ar amphibole (±1σ)	Pavlides and others (1994)
292 to 274.1	^{40}Ar/^{39}Ar microcline	Pavlides and others (1994)
	Burkeville	
295-312	U-Pb zircon	Horton and others (1995)[c]
	Morefield Mine pegmatite mineral ages	
416±21	K-Ar albite (blocky blue)	Laughlin (1968)[c]
357.1±4.9	^{238}U-^{206}Pb monazite LA-ICP-MS	Peterman and others (2006)[c]
327±16	Th-Pb monazite SIMS	Peterman and others (2006)[c]
297±9	K-Ar albite (moonstone)	Laughlin (1968)[c]
289±14	Rb-Sr muscovite	Deuser and Herzog (1962)
274.58±0.58	^{238}U-^{206}Pb monazite ID-TIMS	Peterman and others (2006)[c]
275±1	^{238}U-^{206}Pb monazite CA-TIMS (±2σ)	Peterman and others (2012)
270±13	Rb-Sr muscovite	Deuser and Herzog (1962)
262.1±4.1	Th-Pb monazite LA-ICP-MS	Peterman and others (2006)[c]
261±13	Rb-Sr muscovite	Deuser and Herzog (1962)
261±3	^{238}U-^{206}Pb monazite LA-ICP-MS (±2σ)	Kohn and Vervoort (2008)
254.0±3.4	^{238}U-^{206}Pb monazite ID-TIMS (±2σ)	Kohn and Vervoort (2008)
253.5±4.3	^{238}U-^{206}Pb monazite ID-TIMS (±2σ)	Kohn and Vervoort (2008)
252.9±2.0	^{238}U-^{206}Pb monazite ID-TIMS (±2σ)	Kohn and Vervoort (2008)
248±4	K-Ar muscovite	Laughlin (1966)[c], (1968)[c]
246±2	^{232}Th-^{208}Pb and ^{235}U-^{207}Pb monazite LA-ICP-MS (±2σ)	Kohn and Vervoort (2008)

[a] Figure 1 shows the locations of plutons.

[b] Method includes approach and level of uncertainty, if reported. CA-TIMS = Multi-step Chemical Abrasion Thermal Ionization Mass Spectrometry, ID-TIMS = Isotope Dilution Thermal Ionization Mass Spectrometry, LA-ICP-MS = Laser Ablation Inductively Coupled Plasma Mass Spectrometry, SIMS = Secondary Ion Mass Spectrometry.

[c] Age reported in a conference abstract, regional field guide, thesis, or dissertation.

The origin of common Pb in monazite is speculated as secondary, variably hosted in fractures, along grain boundaries, as surface contamination, or derived from residual monazite-forming fluids, rather than primary within the mineral structure (Hoisch and others, 2008; Janots and others, 2012; Seydoux-Guillaume and others, 2012). Unlike zircon ($ZrSiO_4$), monazite can recrystallize in association with hydrothermal fluids during subsequent metamorphic events (Janots and others, 2012; Seydoux-Guillaume and others, 2012; Upadhyay and Pruseth, 2012; Wawrzenitz and others, 2012; Didier and others, 2013), and thereby alter its primary texture and composition (Harlov and others, 2011). Accordingly, fluid-rock reactions that occur after monazite crystallization may account for secondary enrichment in common Pb (Janots and others, 2012; Didier and others, 2013), in addition to other elements. If a secondary mechanism accounts for common Pb enrichment in the Amelia monazite, detailed spatial analysis of major and trace element distributions within monazite crystal domains may identify regions where U-Th-Pb geochronology methods may best constrain crystallization by targeting the least-altered portions of the grain.

Herein, we spatially analyze a single, mm-sized monazite grain from the Morefield Mine pegmatite district in Virginia (figs. 1 and 2) for its major and trace element contents, using both EPMA (n = 64) and LA-ICP-MS (n = 58). We also use backscattered electron (BSE) imagery to assess relative compositional variations across the grain. The principal goal of these efforts was to delineate the spatial distribution of common Pb and related elements. With this base, we apply secondary ion mass spectrometry (SIMS), a technique that combines high spatial resolution with high mass resolving power for isotopic measurements, to derive ^{232}Th-^{208}Pb ages (n = 59), and assess the results in relation to the regional and local geologic framework. For consistency with previous isotopic and chemical studies of this specimen, we refer to the study sample as the "Amelia monazite" (Kohn and Vervoort, 2008; Peterman and others, 2012).

GEOLOGICAL BACKGROUND

Monazite in Amelia County, Virginia was first described in the late 19th century (Koenig, 1882; Penfield, 1882; Fontaine, 1883). It occurs as single, amber-colored, flattened crystals (consistent with a primary growth texture) interlocked with tantalite-Mn ($MnTa_2O_6$) (Glass, 1935) and cleavelandite albite within silicate replacement bodies of the Morefield Mine pegmatite (Kearns, 1993). Monazite crystals from this area, some in 6.8 to 9.0 kg aggregates (Fontaine, 1883), were among the first targeted for quantitative chemical analysis to understand the mineral's composition and substitution mechanisms (Penfield, 1882; Murata and others, 1953). Morefield Mine opened in 1929 to exploit a wide variety (>80) of pegmatite minerals, of which monazite is rare (Glass, 1935; Kearns, 1993). Monazite is more common in the nearby (~1 mile) Rutherford mines in association with microlite [$(Na,Ca)_2Ta_2O_6$], in aggregate masses as heavy as 3.6 kg (Glass, 1935; Kearns, 1993).

The Amelia monazite is part of the Morefield Mine pegmatite, which consists of a series of dikes, lenticular bodies, lenses, and lit-par-lit structures emplaced along NW striking fractures (fig. 1) (Taber, 1913; Pegau, 1932; Lemke and others, 1952, 1953; Sinkankas, 1968; Kearns, 1993; Smerekanicz and Dudas, 1999). The main pegmatite body exposure (~360m long and ~16-100m wide; Smerekanicz and Dudas, 1999; Kearns, 1993) has been extensively studied for mineralogy (Glass, 1935; Lemke and others, 1952, 1953; Sinkankas, 1968; Kearns, 1995; Lumpkin, 1998; Smerekanicz and Dudas, 1999; Kearns and Martin, 2000). These studies document over 100 different mineral species within the pegmatite, including commercial gems, rare earth minerals, commercial quantities of mica, and rare aluminum-fluoride minerals (Kearns, 1995).

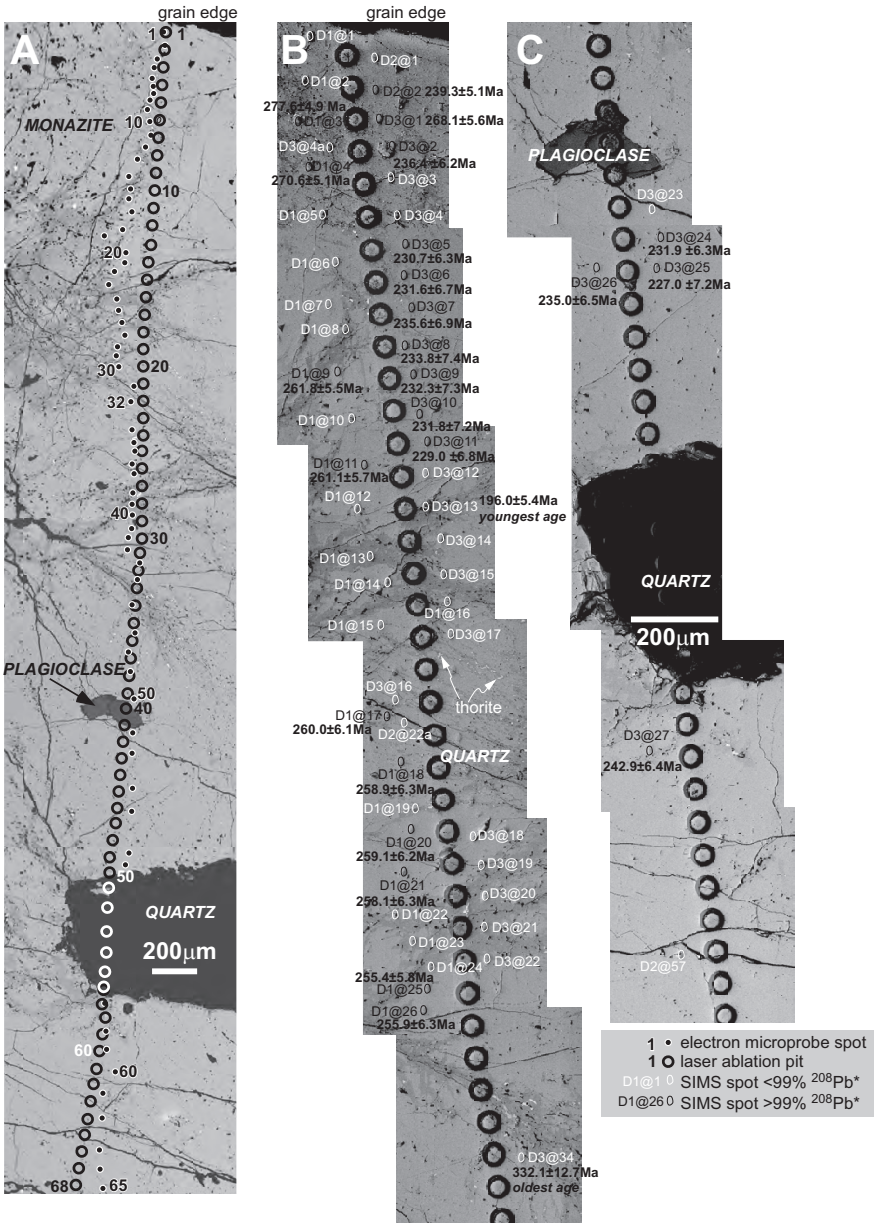

Fig. 2. High-contrast backscattered electron (BSE) image of the Amelia monazite grain. (A) Approximate locations of EPMA and laser spots are indicated with some spot numbers labeled for reference. Inclusions are quartz and plagioclase. (B and C) Higher magnification images of the same region taken after LA-ICP-MS and SIMS analysis. Locations of SIMS spots indicated with some ages indicated. See tables 5 and 6 for ages and isotopic data.

Radiometric dating methods applied to Morefield Mine pegmatite minerals yield a wide range of ages that differ by ~170 myrs (table 1). Amelia monazite ages obtained using LA-ICP-MS range from 357.1±4.9 Ma (^{238}U-^{206}Pb) to 246±2 Ma (^{232}Th-^{208}Pb and ^{235}U-^{207}Pb monazite) (table 1). A spread of muscovite Rb-Sr ages (289±14 Ma,

270±13 Ma, and 261±13 Ma) has been interpreted to reflect a redistribution of Sr during metamorphism (Deuser and Herzog, 1962; Smerekanicz and Dudas, 1999). Mica and albite K-Ar ages obtained from the same locality are also complicated (Laughlin, 1966, 1968; Smerekanicz and Dudas, 1999); three muscovite ages average 248±4 Ma, whereas two albite ages are 416±21 Ma (blocky blue albite) and 297±9 Ma (moonstone variety) (Laughlin, 1966; Laughlin, 1968).

The diversity of radiometric ages determined from Morefield Mine pegmatite minerals and the lack of stratigraphic exposure hamper a clear understanding of how pegmatite emplacement relates to its broader tectonic setting (Smerekanicz and Dudas, 1999). The pegmatite intrudes the Maidens Gneiss, part of the Goochland Terrane (fig. 1) (Farrar, 1984; Smerekanicz and Dudas, 1999; Spears and others, 2004). The Goochland terrane has a debated origin. Labeled as an enigmatic crustal block in the Southern Appalachians (Owens and others, 2010; Martin and Owens, 2012), the terrane may be a Grenvillian fragment juxtaposed along the Piedmont Terrane during Paleozoic orogenic events, a displaced Laurentian or peri-Gondwanan fragment, or some other exotic terrane (Glover, 1989; Horton and others, 1989; Glover and others, 1995; Keppie and others, 1996; Bartholomew and Tollo, 2004; Bailey and others, 2005). The Maidens Gneiss may be derived from an igneous protolith that originated in a Devonian arc (Owens and others, 2010, 2015). Devonian zircon ages from the unit are interpreted to time crystallization (403.3±0.25 Ma to 382.4±0.46 Ma, ±1σ, $^{206}Pb/^{207}Pb$ isotope dilution (ID)-TIMS; Owens and others, 2010, 2015). Mesoproterozoic zircon ages are also reported, and consistent with an older igneous history (1035±5 Ma, Horton and others, 1995; Spears and others, 2004). Analyses of the Devonian zircons yield upper intercepts on concordia at 1086±210 Ma and 955±430 Ma [±1σ, and whole grain methods, chemical abrasion (CA)-TIMS, Owens and others, 2010].

Magmatic fluids sourcing the Morefield Mine pegmatite have been linked to the Columbia pluton (Taber, 1913; Farrar, 1984), the Red Oak granite (Lemke and others, 1953; Laughlin, 1973), and a small biotite granite within the Chopawamsic Terrane (fig. 1) (see discussion in Spears and others, 2004). These, and other proximal candidates (Burkeville, Buggs Island, and Ellisville plutons, fig. 1) are Late Ordovician to Pennsylvanian in age (table 1), but numeric age constraints are sparse and limited mainly to conference abstracts. However, radiometric ages of most minerals within the Morefield Mine pegmatite appear younger than nearby intrusions (table 1) and other regional pegmatites (Devonian to Carboniferous, see review in Smerekanicz and Dudas, 1999). Permian $^{40}Ar/^{39}Ar$ microcline ages from the Ellisville pluton (292 Ma and 274.1 Ma) are within the range of ages reported from the monazite, but the majority of radiometric dates from this intrusion are Silurian to Devonian (table 1). Pavlides and others (1994) speculate that the younger ages from the Ellisville pluton reflects regional cooling due to erosion rather than primary crystallization ages.

The Morefield Mine pegmatite could be genetically related to the Petersburg granite (Smerekanicz and Dudas, 1999), a large NNE-trending pluton eastwardly adjacent to the Goochland Terrane and in direct contact with the terrane along the NE-trending Hylas Fault (fig. 1A). Because episodes of fault displacement were accompanied by magma intrusion, dates obtained for the granite have been used to constrain the timing of transpressional motion within the Hylas Fault (Gates and Glover, 1989; Buchwaldt and Owens, 2012). A Mississippian (330±8 Ma) U-Pb zircon age from the granite has been commonly cited as a prospective constraint on initial granite emplacement and fault activity (Wright and others, 1975; Bobyarchick and Glover, 1979; Gates and Glover, 1989). However, more recent ID-TIMS U-Pb zircon ages from texturally distinct portions of the pluton are ~30 myrs younger at 300.08±0.10

Ma for porphyritic regions and 296.33±0.11 Ma for massive, medium grained regions (table 1; Buchwaldt and Owens, 2012).

METHODS

Sample Preparation

The Amelia monazite sample analyzed here is a split from a Morefield Mine pegmatite sample obtained commercially and previously analyzed for U-Th-Pb geochronology by Kohn and Vervoort (2008). To minimize common Pb contamination, our sample preparation protocol is similar to that described in Catlos and others (2002) for *in situ* monazite SIMS analysis. A single, large (several mm-sized) monazite grain was embedded in a 1-inch epoxy round (Beuhler, EpoxiCure 2 Epoxy System). After curing, the monazite-side of the mount was sanded (sandpaper) and polished smooth (Mother's Billet Metal Polish). The back of the mount was then removed using a high-precision saw to leave the sample mount with a final thickness of ~5mm. To remove surface contamination from the polished monazite surface (polishing compound, saw cutting fluid – Allied Low Speed Cutting Fluid) the mount was ultrasonically cleaned in Buehler cleaning agent for 5 minutes followed by 15 minutes in pure distilled water. The monazite grain mount was coated in carbon for initial EPMA and SEM imaging. For LA-ICP-MS analysis the carbon coat was removed using Mother's Billet Metal Polish, followed by the former cleaning procedure. For SIMS analysis the surface was again cleaned using the standard procedure and then gold-coated. Both LA-ICP-MS and SIMS involved pre-sputtering prior to data collection.

Electron Microprobe Analysis

The monazite grain was initially imaged in high contrast BSE mode to reveal its zoning and select transects for quantitative analysis (figs. 2 and 3). Following compositional (EPMA, LA-ICP-MS) and geochronological (SIMS) analyses, the grain was re-imaged in BSE and secondary electron (SE) modes to document textures and zonation associated with individual analytical spots. The EPMA transect across the Amelia monazite grain was performed at University of Oklahoma using a CAMECA SX50 electron probe micro-analyzer equipped with five wavelength dispersive X-ray spectrometers, an integrated energy-dispersive X-ray analyzer, and standard SEM imaging capabilities. Because monazite can incorporate a wide variety of elements into its structure, obtaining normative compositions by EPMA can be challenging (Montel and others, 1996; Hetherington and others, 2008). Analytical protocols followed methods developed by Hetherington and others (2008) and George Morgan (personal communication) for xenotime with the exception that Pb was analyzed using the Mα emission rather than Mβ. Table 2 lists the elements, X-ray emissions, diffracting crystals, and standards used for analyses.

The electron microprobe operated at a 20kV accelerating voltage, 20nA current and a 2μm spot size. Counting times were 30 seconds on peak for all elements, except Mg and Si, which were 60 seconds each. An overlap correction was applied for the Pr Lγ emission on the Eu Lα line using the Pr-bearing Rare Earth Phosphate standard-2 (REP2; George Morgan, personal communication). Each spot analysis required ~15 minutes. Overall, we obtained 64 spot analyses located ~20μm apart across the grain, with 46 on the lighter BSE regions of the grain and 18 on darker BSE regions (fig. 2). The instrument was stable (<0.2 nA beam current drift, laboratory temperature variation <1°C) during the 19 hour session, thus standards were only analyzed at the beginning. EPMA compositional data, after normalization to 4 oxygens, fit monazite stoichiometry (table 3, fig. 4, supplementary data, http://earth.geology.yale.edu/%7eajs/SupplementaryData/2016/01Catlos.xlsx).

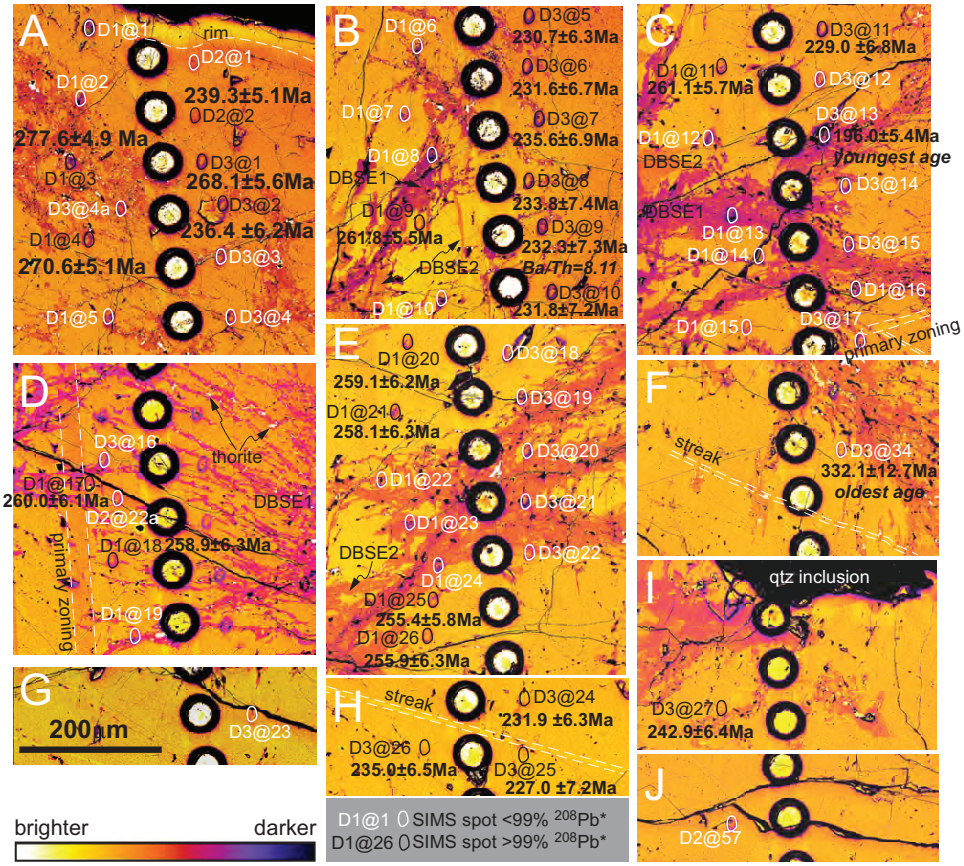

Fig. 3. (A-J) Color, high-contrast BSE images of portions of the Amelia monazite grain to show SIMS spot details. Spots are labeled for reference. Ages ($\pm 1\sigma$) are indicated only for spots with >99% ^{208}Pb*. Thorite inclusions and regions of darker BSE generations are labeled (DBSE1 = darker BSE generation 1; DBSE2 = darker BSE generation 2). Some sector zoned regions and streaks are shown by dashed lines. Color scale is qualitatively labeled from bright to dark contrast.

LA-ICP-MS Analysis

We measured lower concentration minor and trace element constituents of the Amelia monazite using LA-ICP-MS at the University of Texas at Austin. The system consists of a New Wave UP193fx (193nm, 4-6ns pulse width) excimer laser coupled to an Agilent 7500ce ICP-MS. The laser spot traverse was positioned closely parallel to the earlier-run EPMA grain transect (fig. 2). Laser ablation parameters optimized from representative Amelia monazite test ablations, were 60s ablations using a 50µm diameter spot size at 50 percent power (fluence of 5.2 J/cm^2), 10 Hz repetition rate, and a He cell flow of 250 mL/min. Pulse-to-pulse laser power variation was <3.7 percent over the analysis period. All spots were pre-ablated for 2s using a 75µm spot, 20 percent laser power, and 10 Hz repetition rate to remove surface contamination. The quadrupole time-resolved method involved measurement of 22 analytes at 1 point per spectral peak, using the integration times of 10ms (^{31}P, ^{89}Y), 20ms (^{23}Na, ^{27}Al, ^{47}Ti, ^{55}Mn, ^{57}Fe, ^{75}As, ^{137}Ba, ^{153}Eu, ^{157}Gd, ^{159}Tb, ^{163}Dy, ^{165}Ho, ^{166}Er, ^{169}Tm, ^{172}Yb, ^{175}Lu) and 30ms (^{204}Pb, ^{208}Pb, ^{232}Th, ^{238}U). The resulting sampling period (0.5062s) corresponded to >90 percent detection time, enabling 118 measurements to be made

TABLE 2

Conditions used for EPMA monazite compositional analysis[a]

Element	Crystal	X-ray Line	Background high	Background low
Si	TAP	Kα	+0.00650	-0.00700
Y	TAP	Lα	+0.00550	-0.00550
U	PET	Mβ	+0.00750	-0.01000
Pb	PET	Mα	+0.00450	-0.00800
P	PET	Kα	+0.01503	-0.01313
S	PET	Kα	+0.00506	-0.00378
Th	PET	Mα	+0.00400	-0.00500
Fe	LIF	Kα	+0.00750	-0.00850
As	LIF	Kα	+0.00597	-0.00530
La	LIF	Lα	+0.00600	-0.00600
Ce	LIF	Lα	+0.01000	-0.01000
Pr	LIF	Lβ	+0.00473	-0.00369
Nd	LIF	Lα	+0.00600	-0.01000
Sm	LIF	Lβ	+0.00806	-0.01187
Eu	LIF	Lα	+0.00799	-0.00800
Gd	LIF	Lβ	+0.01552	-0.01322
Tb	LIF	Lα	+0.00813	-0.06270
Ca	PET	Kα	+0.00500	-0.00500
Na	TAP	Kα	+0.01200	-0.01200
Ti	LIF	Kα	+0.01000	-0.00700
Mn	LIF	Kα	+0.00650	-0.00600
Al	TAP	Kα	+0.00800	-0.00800
Mg	TAP	Kα	+0.00870	-0.00870
F	TAP	Kα	+0.00850	-0.00850
Cl	PET	Kα	+0.00800	-0.00800

[a] Standards for the REE are ternary rare earth orthophosphates (REP) described by Hetherington and others (2008). Durango fluorapatite (Young and others, 1969) was used for Ca, galena for Pb, synthetic ThO_2 and depleted pure uranium metal (C.M. Taylor Corp.) for Th and U. Natural and synthetic crystalline solids were used for the remaining elements.

within the dwell interval (60s), conditions suitable for robust measurement (Longerich and others, 1996). A 45s gas blank interval was used between all laser measurements. Monazite analyses were bracketed hourly by triplicate analyses of laser ablation standards NIST-612 and NIST-610 (Jochum and others, 2011) and USGS MAPS-4. MAPS-4 is a synthetic trace element-doped calcium phosphate [$(Ca_3(PO_4)_2$] precipitate (Neymark and others, 2014), with a P content (16.7±1.7 wt.%) similar to monazite (11.94 wt.% from EPMA). See D'Oriano and others (2008) and Xu and others (2000) for evaluations of the quality of the NIST-612 and NIST-610 glasses. Measured analyte intensities were converted to elemental concentrations using Iolite software (Hellstrom and others, 2008), with MAPS-4 as the primary calibration standard and ^{31}P as the internal standard reference. Amelia monazite P concentration was assigned based on average EPMA P_2O_5 analyses.

Average analyte recoveries on external standards were better for NIST-610 (128%) than NIST-612 (156%), but we consider these worst-case accuracy estimates considering the P contents of these standards are ~5000 and ~30,000 times lower than MAPS-4. Analyte concentrations for monazite ablations were predominantly 100 to 1000 of times higher than estimated detection limits; intensities for ^{204}Pb were 40 to 155 times higher than background levels. We report ^{204}Pb and ^{208}Pb contents in ppm, which have larger uncertainty because Pb is not a stable isotope system. These

TABLE 3

Average EPMA Amelia monazite compositions

Oxide[a]	All Amelia (wt.%)[b]	Lighter (wt.%)[c]	Darker (wt.%)[d]
P_2O_5	27.39 (0.58)	27.16 (0.32)	27.96 (0.67)
As_2O_5	0.06 (0.06)	0.05 (0.05)	0.08 (0.07)
SiO_2	1.60 (0.36)	1.75 (0.17)	1.21 (0.43)
TiO^2	0.01 (0.01)	0.01 (0.01)	0.01 (0.01)
ThO_2	8.43 (1.41)	8.98 (0.75)	7.04 (1.68)
UO_2	0.35 (0.14)	0.40 (0.08)	0.23 (0.18)
Al_2O_3	0.01 (0.01)	0.01 (0.01)	0.01 (0.01)
Y_2O_3	1.56 (0.38)	1.70 (0.14)	1.20 (0.53)
La_2O_3	10.55 (0.40)	10.45 (0.33)	10.79 (0.44)
Ce_2O_3	30.68 (1.00)	30.32 (0.60)	31.61 (1.19)
Pr_2O_3	3.51 (0.17)	3.47 (0.14)	3.61 (0.18)
Nd_2O_3	12.39 (0.42)	12.21 (0.22)	12.85 (0.45)
Sm_2O_3	1.19 (0.11)	1.17 (0.10)	1.23 (0.09)
Eu_2O_3	0.11 (0.05)	0.11 (0.05)	0.11 (0.04)
Gd_2O_3	0.41 (0.08)	0.41 (0.08)	0.41 (0.08)
Tb_2O_3	0.01 (0.01)	0.01 (0.01)	<0.01%
CaO	0.57 (0.04)	0.57 (0.04)	0.59 (0.04)
F	0.87 (0.09)	0.88 (0.09)	0.85 (0.09)
Cl	0.05 (0.01)	0.05 (0.01)	0.05 (0.01)
O=F	-0.37 (0.04)	-0.37 (0.04)	-0.36 (0.04)
O=Cl	-0.01 (0.00)	-0.01 (0.00)	-0.01 (0.00)
Total	99.36 (0.47)	99.32 (0.41)	99.48 (0.58)
apfu			
P	0.935 (0.015)	0.929 (0.007)	0.950 (0.018)
As	0.001 (0.001)	0.001 (0.001)	0.002 (0.002)
Si	0.064 (0.015)	0.071 (0.007)	0.049 (0.017)
Ti	<0.001	<0.001	<0.001
Th	0.077 (0.013)	0.083 (0.007)	0.064 (0.016)
U	0.003 (0.001)	0.004 (0.001)	0.002 (0.002)
Al	<0.001	<0.001	<0.001
Y	0.034 (0.008)	0.037 (0.003)	0.026 (0.011)
La	0.157 (0.005)	0.156 (0.005)	0.160 (0.006)
Ce	0.453 (0.013)	0.448 (0.008)	0.464 (0.016)
Pr	0.052 (0.002)	0.051 (0.002)	0.053 (0.002)
Nd	0.178 (0.005)	0.176 (0.003)	0.184 (0.006)
Sm	0.016 (0.001)	0.016 (0.001)	0.017 (0.001)
Eu	0.001 (0.001)	0.001 (0.001)	0.001 (0.001)
Gd	0.005 (0.001)	0.005 (0.001)	0.005 (0.001)
Tb	<0.001	<0.001	<0.001
Ca	0.025 (0.002)	0.025 (0.002)	0.026 (0.002)
F	0.111 (0.012)	0.112 (0.012)	0.108 (0.011)
Cl	0.004 (0.001)	.004 (0.001)	0.004 (0.001)
Sum	2.003 (0.002)	2.003 (0.002)	2.003 (0.002)

[a] Data normalized to 4 oxygens. Supplementary 1 data contains details regarding the standard (http://earth.geology.yale.edu/%7eajs/SupplementaryData/2016/01Catlos.xlsx). Measured but not detected: FeO, MnO, MgO, Na_2O, SO_3, and PbO.

[b] Averages include 64 spot analyses. See figure 2 for locations.

[c] A total of 46 analyses were made on the lighter region of the grain.

[d] A total of 18 analyses were made on the darker region of the grain.

concentrations are accordingly only used to gauge relative amounts of common (^{204}Pb) versus radiogenic (^{208}Pb*) Pb in proximity to possible secondary features (microcracks, dark BSE regions) as compared to the bulk grain. Although a possible

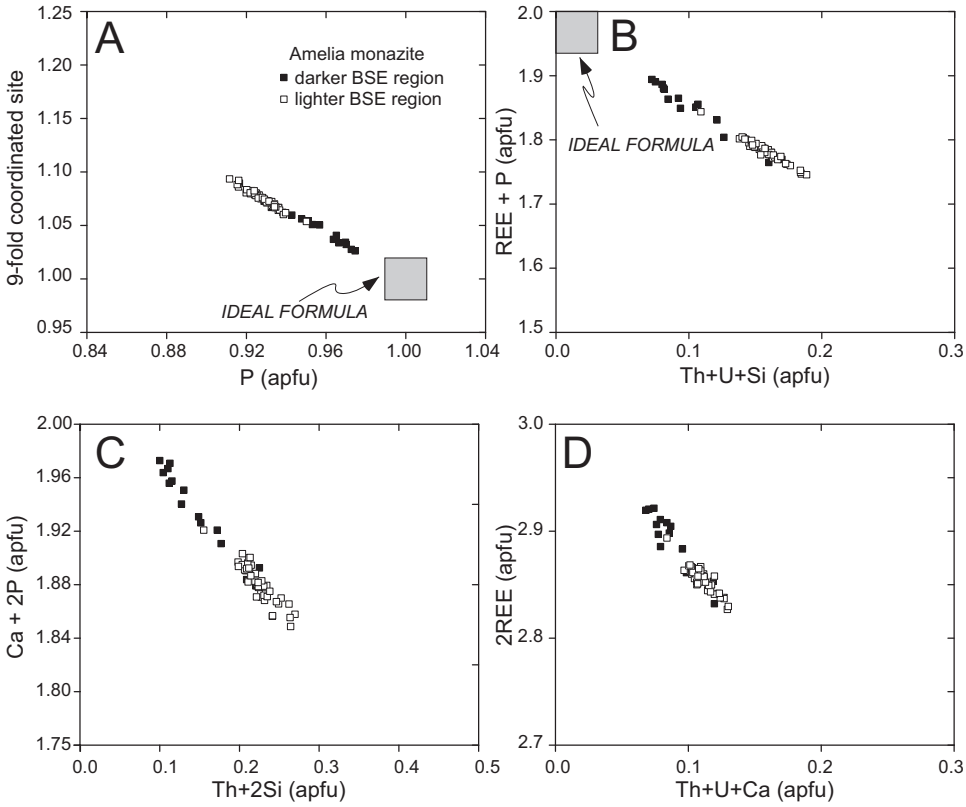

Fig. 4. Plots of Amelia monazite EPMA compositions. (A) P (atoms per formula unit, apfu) vs. elements located in the 9-fold coordinated site in monazite. (B) Th + U + Si (apfu) vs. REE + P (apfu). Boxes in panels (A) and (B) indicate the region of ideal monazite formula. (C) Plot of Th + 2Si vs. Ca + 2P and (C) Th + U + Ca (apfu) vs. 2REE (apfu). REEs in panels (B) and (D) are La, Ce, Pr, Nd, Sm, Eu, Gd, and Tb. White boxes indicate the electron microprobe spot overlaps a lighter region in BSE, whereas black boxes indicate the spot overlapped a darker region in BSE.

isobaric overlap exists with ^{204}Pb and ^{204}Hg, the un-interfered isotope ^{202}Hg yielded background counts during the analytical session. Table 4 summarizes the LA-ICP-MS data for the Amelia monazite.

Following LA-ICP-MS, the spot transect was re-imaged in secondary electrons (SE) to identify ablation craters that intersected secondary alteration features (deformation textures, microcracks >5μm in width). Regions with microcracks were examined to compare pre- and post-ablation to ascertain if their origin was intrinsic or laser-induced (fig. 5). Efforts to compare EPMA and LA-ICP-MS compositional data where spots were acquired in close proximity proved impractical because the larger laser spot size (~50μm compared to ~2μm EPMA) occasionally overlapped zones of varying BSE brightness or more than one EPMA analysis.

Ion Microprobe (SIMS) Analysis

The Amelia monazite was dated by Th-Pb geochronology using the UCLA CAMECA ims1270 ion microprobe (figs. 2 and 3; tables 5 and 6). In this method, a focused ~30μm diameter oxygen ion beam sputters ions of individual atoms and secondary oxide molecules from the sample surface, which are separated in a magnetic

TABLE 4

Average EPMA Amelia monazite compositions

	Amelia (ppm, ±2σ)[a]	Microcracks visible (ppm, ±2σ)[b]	No microcracks visible (ppm, ±2σ)[c]
^{232}Th	122,295 (3935)	119,850 (3950)	126,290 (4750)
^{89}Y	25,295 (810)	24,630 (810)	26,385 (985)
^{157}Gd	11,620 (470)	11,595 (465)	11,660 (595)
^{163}Dy	3800 (130)	3745 (125)	3885 (165)
^{238}U	2590 (100)	2420 (100)	2870 (130)
^{208}Pb	2765 (140)	3005 (165)	2375 (115)
^{57}Fe	1650 (270)	2470 (335)	300 (190)
^{159}Tb	1085 (40)	1080 (40)	1095 (50)
^{166}Er	815 (35)	795 (35)	845 (40)
^{75}As	575 (20)	580 (20)	570 (20)
^{172}Yb	475 (20)	475 (25)	470 (20)
^{204}Pb	450 (85)	700 (105)	40 (40)
^{165}Ho	395 (15)	385 (15)	405 (20)
^{27}Al	220 (30)	345 (35)	20 (20)
^{153}Eu	120 (5)	120 (5)	120 (5)
^{137}Ba	45 (9)	69 (11)	5 (4)
^{23}Na	32 (6)	32 (5)	30 (7)
^{175}Lu	39 (3)	40 (3)	37 (2)
^{55}Mn	12 (4)	13 (4)	12 (6)

[a] Average (ppm, ±2σ) of all Amelia monazite analyses (n = 58). The uncertainty is the standard error statistic (2σ/square root of n), where n is the number of quadrupole cycles completed within the dwell interval (time laser is firing on the sample). The magnitude of the uncertainty scales with concentration. Data is rounded to the nearest 5 ppm for values above 100 ppm and to the nearest 1 ppm for values below 100 ppm. See supplementary data for analytical details.

[b] Average (ppm, ±2σ) compositions of regions where the laser was placed on regions of the Amelia monazite with visible microcracks (n = 22).

[c] Average (ppm, ±2σ) compositions of regions where the laser was placed on regions of the Amelia monazite with no visible microcracks (n = 36).

sector and counted by an array of detectors. Prior to analysis, the sample surface is visible as a reflected light image from which the earlier LA-ICP-MS spot transects could be seen. Although areas of secondary alteration (other than microcracks) were not distinguishable in reflected light view, based on earlier imagery, we targeted sample areas of secondary alteration in addition to unaltered grain areas for geochronology. The analyte ions measured included $^{208}Pb^+$, $^{206}Pb^+$, $^{207}Pb^+$, $^{204}Pb^+$, $^{232}Th^+$, $^{248}ThO_2^+$, $^{235}U^+$, $^{238}U^+$ and $^{254}UO^+$. Prior to ion counting over 15 minute intervals, the grain was pre-sputtered for 20 seconds to remove a conductive gold coating and any potential contaminants. Analyte intensity data obtained over the course of three days, with the majority of data collected on days 1 and 3. The monazite 554 reference age standard was used to develop the ThO_2^+/Th^+ vs. Pb^+/Th^+ calibration lines, the slope and intercept of which are controlled by the age of the standard (fig. 6; table 7) (see

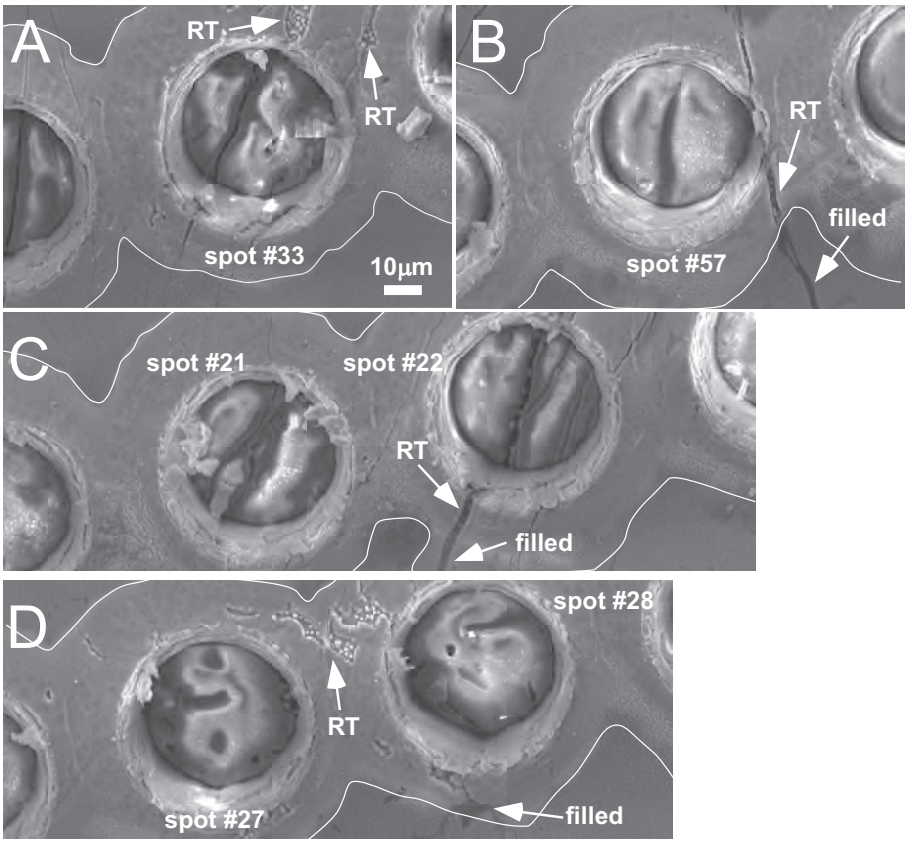

Fig. 5. Secondary electron (SE) images of LA-ICP-MS spots on the Amelia monazite. Spot numbers are indicated. White lines outline lighter BSE haloes surrounding the spots. RT = recrystallization textures; filled = microcracks with darker material.

Harrison and others, 1995, 1999; Catlos and others, 2002). Monazite 554 has yielded ages of 46±1 Ma, 45.3±1.4 Ma, and 45±1 Ma (±2σ, see discussion in Harrison and others, 1999). The level of accuracy and precision we obtained from the same standard is consistent with these results (table 7).

In addition to the isotopes for geochronology, we also measured $^{137}Ba^{+}$ on days 2 and 3, based on LA-ICP-MS analyses that suggested spatial covariation of ^{137}Ba with ^{204}Pb within altered regions of the Amelia monazite grain (see further discussion). The peak was first identified using NIST610 glass, which has 435±23 ppm Ba (Jochum and Nohl, 2008). To avoid overlap of potential Ba-related polyatomic interferences on Pb isotopes (table 8), the ion microprobe operated at a mass resolving power (MRP) ~5000. Tables 5 and 6 report $^{137}Ba^{+}/^{232}Th^{+}$ and $^{137}Ba^{+}/^{238}U^{+}$ for ages obtained during days 2 and 3.

Each SIMS spot was re-imaged by SEM at the University of Texas at Austin, Bureau of Economic Geology to identify any spots intersecting aberrant areas of the monazite grain surface such as microcracks or pits, darker BSE regions, or inclusions (tables 5 and 6). It was impossible to avoid sub-micron scale aberrations, but we also deliberately targeted spots within visibly altered areas to see if they were regions comparatively enriched in (common) $^{204}Pb^{+}$. Detailed re-imaging was required as common Pb in the

TABLE 5

SIMS analytical data from the Amelia monazite with $\%^{208}Pb^* > 99\%$

Day spot@#[a]	^{232}Th-^{208}Pb age (Ma,±1σ)[b]	$^{137}Ba^+/Th^+$ (x10^{-4}, ±1σ)[c]	$^{137}Ba^+/U^+$ (±1σ)[c]	$\%^{208}Pb^*$ (±1σ)[d]	$^{208}Pb^+/^{232}Th^+$ (x10^{-2}±1σ)[e]	ThO_2^+/Th^+ (±1σ)[f]
Spot located on a lighter BSE region free of flaws[g]						
D1@9	261.8 (5.5)	n.m.	n.m.	99.5 (0.03)	1.304 (0.026)	3.723 (0.017)
D1@18	258.9 (6.3)	n.m.	n.m.	99.5 (0.03)	1.289 (0.031)	3.401 (0.011)
D2@2	239.3 (5.1)	2.56 (0.10)	0.017 (0.001)	99.0 (0.06)	1.191 (0.025)	4.631 (0.010)
D3@26	235.0 (6.5)	0.98 (0.18)	0.006 (0.001)	99.6 (0.04)	1.170 (0.033)	4.808 (0.010)
D3@9	232.3 (7.3)	8.11 (1.89)	0.051 (0.012)	99.6 (0.04)	1.156 (0.036)	4.419 (0.024)
D3@6	231.6 (6.7)	1.81 (0.10)	0.011 (0.001)	99.6 (0.04)	1.152 (0.034)	4.662 (0.021)
D3@5	230.7 (6.3)	0.26 (0.04)	0.002 (<0.001)	99.7 (0.03)	1.148 (0.031)	4.898 (0.024)
D3@11	229.0 (6.8)	0.60 (0.08)	0.003 (<0.001)	99.7 (0.03)	1.140 (0.034)	4.592 (0.022)
Spot located on a flaw[g]						
D1@3	277.6 (4.9)	n.m.	n.m.	99.4 (0.03)	1.383 (0.025)	4.093 (0.062)
D1@4	270.6 (5.1)	n.m.	n.m.	98.5 (0.08)	1.348 (0.025)	3.998 (0.134)
D3@1	268.1 (5.6)	0.36 (0.04)	0.002 (<0.001)	99.7 (0.03)	1.335 (0.028)	6.039 (0.022)
D1@11	261.1 (5.7)	n.m.	n.m.	99.7 (0.02)	1.300 (0.029)	3.654 (0.014)
D1@17	260.0 (6.1)	n.m.	n.m.	99.1 (0.06)	1.295 (0.031)	3.429 (0.019)
D1@20	259.1 (6.2)	n.m.	n.m.	99.6 (0.03)	1.290 (0.031)	3.423 (0.014)
D1@21	258.1 (6.3)	n.m.	n.m.	99.4 (0.03)	1.285 (0.032)	3.347 (0.013)
D1@26	255.9 (6.3)	n.m.	n.m.	99.4 (0.03)	1.274 (0.032)	3.329 (0.012)
D1@25	255.4 (5.8)	n.m.	n.m.	99.6 (0.03)	1.272 (0.029)	3.528 (0.008)
D3@27	242.9 (6.4)	2.28 (0.19)	0.014 (0.001)	99.1 (0.06)	1.209 (0.032)	4.997 (0.013)
D3@2	236.4 (6.2)	4.58 (0.18)	0.026 (0.001)	99.6 (0.04)	1.176 (0.031)	5.013 (0.022)
D3@7	235.6 (6.9)	8.44 (0.38)	0.049 (0.002)	99.6 (0.04)	1.172 (0.034)	4.651 (0.023)
D3@8	233.8 (7.4)	0.89 (0.06)	0.005 (<0.001)	99.6 (0.04)	1.163 (0.037)	4.349 (0.020)
D3@24	231.9 (6.3)	2.27 (0.18)	0.014 (0.001)	99.3 (0.05)	1.154 (0.032)	4.893 (0.012)
D3@10	231.8 (7.2)	1.01 (0.08)	0.006 (<0.001)	99.6 (0.04)	1.153 (0.036)	4.409 (0.020)
D3@25	227.0 (7.2)	8.02 (0.20)	0.046 (0.001)	99.0 (0.07)	1.129 (0.036)	4.347 (0.025)

[a] Nomenclature: D1 = day 1; D2 = day 2; D3 = day 3, @# = analysis on the Amelia monazite. Average of all analyses in the table is 252±12 Ma (±1σ).

[b] ^{232}Th-^{208}Pb age with ±1σ uncertainty. Age calculated using monazite 554 as a standard.

[c] The $^{137}Ba^+/Th^+$ ratio of the monazite grain. For day 1 analyses, we did not take this measurement n.m. = not measured. Average of all analyses in the table is $3.01\times10^{-4} \pm 5.30\times10^{-5}$.

[d] $\%^{208}Pb^*$ = percent radiogenic ^{208}Pb.

[e] Ratio used in the age calculation.

[f] Ideally the ThO_2^+/Th^+ lies within that defined by the calibration.

[g] Flaw includes a microcrack or pit visible in BSE.

Amelia monazite could be the result of the location of the analyses on a microcrack or mineral inclusion, as opposed to intrinsic in the grain.

RESULTS

Monazite Texture

Figure 2 shows grayscale BSE images across the entire monazite grain with the locations of EPMA, LA-ICP-MS, and SIMS analyses. Variations in mineral texture and zoning are best seen in enhanced color (fig. 3). The majority of the grain surface has light BSE contrast, with brightest regions associated with regions having absent or sparse microcrack distributions (fig. 3A). Subtle parallel zones with brighter BSE contrast (<10μm in width) appear to be remnants of primary (sector?) zoning (figs. 3C and 3D). Regions with high microcrack and pit/pore densities are often characterized by irregular localized distributions of darker BSE contrast that trend parallel to

TABLE 6

SIMS analytical data from the Amelia monazite with % ^{208}Pb < 99%*

Day spot@#[a]	^{232}Th-^{208}Pb age (Ma,±1σ)[b]	^{137}Ba$^+$/ Th$^+$ (x10^{-4}, ±1σ)[c]	^{137}Ba$^+$/ U$^+$ (±1σ)[c]	%^{208}Pb* (±1σ)[d]	^{208}Pb$^+$/^{232}Th$^+$ (x10^{-2}±1σ)[e]	ThO$_2^+$/Th$^+$ (±1σ)[f]
D2@34	332.1 (12.7)	64.4 (2.6)	0.043 (0.002)	98.1 (0.1)	1.657 (0.064)	3.734 (0.009)
D1@1	281.9 (4.2)	n.m.	n.m.	97.0 (0.05)	1.405 (0.021)	4.722 (0.038)
D1@19	265.6 (7.4)	n.m.	n.m.	97.4 (0.2)	1.323 (0.037)	3.129 (0.032)
D3@4a	259.8 (10.5)	1623 (38)	2.207 (0.059)	54.9 (0.7)	1.294 (0.053)	3.995 (0.020)
D1@7	258.7 (5.1)	n.m.	n.m.	93.6 (0.1)	1.288 (0.025)	3.936 (0.021)
D1@14	258.0 (28.0)	n.m.	n.m.	44.9 (3.4)	1.285 (0.140)	3.473 (0.069)
D1@15	257.9 (5.8)	n.m.	n.m.	92.9 (0.4)	1.284 (0.029)	3.484 (0.018)
D1@5	257.9 (10.1)	n.m.	n.m.	61.2 (1.6)	1.284 (0.051)	3.942 (0.010)
D1@22	251.5 (5.4)	n.m.	n.m.	90.1 (0.2)	1.252 (0.027)	3.711 (0.021)
D1@12	248.9 (7.7)	n.m.	n.m.	77.1 (1.3)	1.239 (0.038)	3.558 (0.023)
D1@2	246.9 (16.4)	n.m.	n.m.	46.4 (2.1)	1.229 (0.082)	4.271 (0.035)
D2@1	240.7 (6.9)	63.2 (1.6)	0.041 (0.001)	95.8 (0.1)	1.198 (0.035)	4.967 (0.056)
D1@10	237.3 (11.9)	n.m.	n.m.	33.9 (1.2)	1.181 (0.059)	3.502 (0.02)1
D1@24	234.0 (5.2)	n.m.	n.m.	87.1 (0.2)	1.164 (0.026)	3.842 (0.010)
D3@23	233.9 (6.8)	451 (10)	0.278 (0.006)	83.0 (0.3)	1.165 (0.034)	4.671 (0.017)
D1@6	233.3 (8.1)	n.m.	n.m.	40.0 (0.9)	1.161 (0.041)	3.774 (0.015)
D3@19	231.8 (7.1)	47.5 (1.6)	0.027 (0.001)	98.2 (0.1)	1.154 (0.035)	4.512 (0.013)
D3@18	231.8 (13.3)	860 (82)	0.525 (0.002)	98.4 (0.1)	1.153 (0.067)	4.279 (0.142)
D1@16	231.4 (10.6)	n.m.	n.m.	53.7 (2.0)	1.151 (0.053)	3.251 (0.040)
D2@57	230.3 (5.1)	185 (3)	0.113 (0.002)	93.5 (0.2)	1.146 (0.026)	4.561 (0.013)
D3@3	229.6 (6.8)	350 (20)	0.206 (0.012)	86.0 (0.7)	1.142 (0.034)	5.008 (0.018)
D3@12	228.8 (7.2)	24.0 (1.1)	0.014 (0.001)	97.5 (0.1)	1.138 (0.036)	4.382 (0.020)
D3@4	228.6 (6.5)	320 (4)	0.197 (0.003)	85.8 (0.2)	1.138 (0.033)	4.727 (0.031)
D1@23	226.9 (5.0)	n.m.	n.m.	78.9 (0.4)	1.129 (0.025)	3.947 (0.022)
D3@17	226.9 (6.7)	77.8 (3.6)	0.050 (0.002)	96.5 (0.2)	1.129 (0.033)	4.647 (0.020)
D3@15	224.8 (6.5)	118 (3)	0.091 (0.002)	97.5 (0.1)	1.118 (0.033)	4.651 (0.025)
D1@13	224.0 (7.7)	n.m.	n.m.	63.1 (0.9)	1.115 (0.038)	3.880 (0.013)
D3@16	220.2 (6.7) 1	95 (7)	0.129 (0.005)	92.4 (0.2)	1.095 (0.034)	4.515 (0.031)
D2@22a	218.6 (4.8)	670 (12)	0.429 (0.008)	76.3 (0.6)	1.087 (0.024)	4.833 (0.010)
D3@14	217.9 (6.5)	1893 (167)	1.311 (0.178)	84.3 (0.4)	1.084 (0.032)	4.657 (0.027)
D3@21	213.9 (6.5)	250 (6)	0.185 (0.006)	82.0 (0.5)	1.064 (0.033)	4.607 (0.021)
D3@20	212.1 (11.4)	3478 (163)	2.429 (0.077)	37.2 (1.2)	1.055 (0.057)	4.196 (0.011)
D3@22	204.6 (8.0)	482 (15)	2.429 (0.077)	84.0 (0.3)	1.018 (0.029)	4.768 (0.014)
D1@8	198.6 (30.1)	n.m.	n.m.	15.0 (1.6)	0.987 (0.150)	3.191 (0.171)
D3@13	196.0 (5.4)	3521 (16)	4.265 (0.086)	38.5 (0.4)	0.974 (0.027)	5.163 (0.030)

[a] Nomenclature: D1 = day 1; D2 = day 2; D3 = day 3, A@# = 1 analysis on the Amelia monazite with the beam placed in close proximity to the lased spot with the same number. If a second analysis was taken near the same spot, it is indicated by an "a" after the number. Average of all analyses in the table is 242±12 Ma (±1σ).

[b] ^{232}Th-^{208}Pb age with ±1σ uncertainty. Age calculated using monazite 554 as a standard.

[c] Observed ratio in the monazite grain. For day 1 analyses, we did not take this measurement; n.m. = not measured. Average ^{137}Ba$^+$/Th$^+$ of all analyses is $9.38\times10^{-3}\pm 5.69\times10^{-4}$.

[d] %^{208}Pb* = percent radiogenic ^{208}Pb.

[e] Ratio used in the age calculation.

[f] Ideally the ThO$_2^+$/Th$^+$ lies within that defined by the calibration.

larger microfracture splays (figs. 2, 3B and 3C). Such darker BSE zones are consistent with secondary overprinting (figs. 3F and 3H); similar textural attributes are described in monazite that experienced dissolution and reprecipitation (Seydoux-Guillaume and others, 2012). Thorite grains (10–100μm grain size) identified using energy dispersive spectrometry (EDS) appear as bright inclusions filling cracks within the darkest BSE generation (figs. 2 and 3). Plagioclase and quartz comprise other larger inclusions

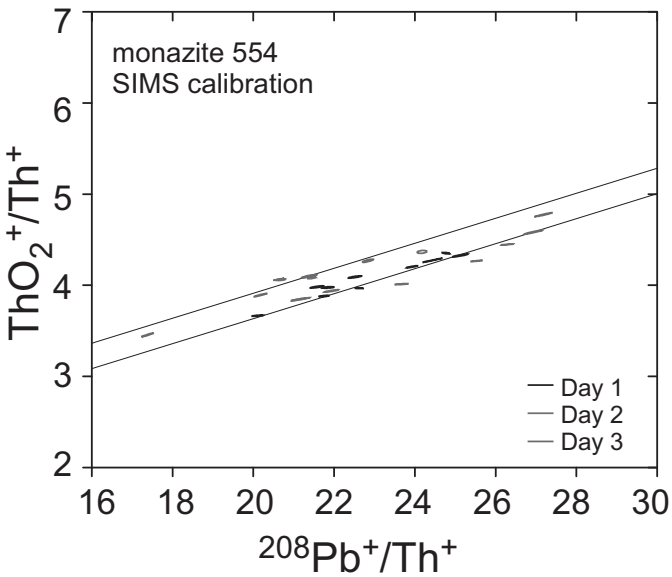

Fig. 6. Monazite calibration curve for ^{232}Th-^{208}Pb. Twenty-six spots were placed on standard monazite 554 over the course of 3 days. See table 7 for calibration data.

within the monazite matrix (fig. 2). Patchy areas with darker BSE contrast are noted in proximity to the larger inclusions (fig. 3I).

Compositional Data

Table 3 reports the average Amelia monazite EPMA compositions for all analyzed spots, and for spots located on regions of bright and darker BSE contrast. Overall, the monazite contains Ce, Nd, and La as its major LREEs and is high in Th (8.54±1.63 wt.%). Common substitution mechanisms in monazite include Th + U + Si → REE + P, Th + 2Si → Ca + 2P, and Th + U + Ca → 2REE (fig. 4). Silica (1.62±0.42 wt.%) likely enters the mineral via huttonite-coupled substitution, whereas CaO (0.60±0.25 wt.%) indicates a minor a brabanite or cheralite component (Burt, 1989). Compositions from darker BSE regions approach ideal monazite stoichiometry relative to bright BSE regions, and have lower concentrations of Si, Th, U, and Y and higher P, REE, and Ca (table 3, figs. 4 and 7).

Table 7

SIMS calibration line data

Day[a]	Slope[b]	Intercept[b]	Number[c]	Monazite 554 age[d]
1	0.139	0.893±0.057	10	44.9±0.8 Ma
2	0.069	2.639±0.042	5	44.6±1.4 Ma
3	0.132	1.189±0.101	6	44.9±1.8 Ma

[a] Day the calibration was generated.
[b] Calibration line has an equation of ThO_2^+/Th^+ = slope (Pb^+/Th^+) + intercept.
[c] Number of spots placed on monazite standard 554.
[d] Age of monazite 554 (±1σ) uncertainty reproduced using the calibration line.

TABLE 8

Possible Ba-related interferences with ^{204}Pb

Interference[a]	Rel. abundance[b]	Mass[c]	Mass difference[d]	MRP[e]
$^{138}Ba^{18}O^{16}O_3$	5.695E-3	203.8891	-0.0839	2431
$^{136}Ba^{18}O_2{}^{16}O_2$	1.876E-6	203.8927	-0.0803	2539
$^{138}Ba^{31}P^{18}O^{17}O$	1.090E-6	203.8773	-0.0957	2130
$^{137}Ba^{18}O^{17}O^{16}O_2$	1.019E-6	203.8939	-0.0791	2579
$^{138}Ba^{17}O_2{}^{16}O_2$	6.183E-7	203.8933	-0.0791	2559
$^{137}Ba^{31}P^{18}O_2$	4.492E-7	203.8779	-0.0950	2144

[a] Potential Ba-bearing isotopic species that interferes with ^{204}Pb.
[b] Relative abundance of this species.
[c] Mass of this species.
[d] Mass difference with ^{204}Pb.
[e] Mass resolving power (MRP) needed to resolve this species from ^{204}Pb. The ion microprobe operates with a MRP ~5000.

The Amelia monazite averages 0.11±0.01 weight percent F, regardless of BSE contrast character. Fluorine is used to charge balance the huttonite substitution (Kuncha, 1980) and is thought to play a factor in the enrichment of high-Th monazites (Watt, 1995). We found no clear relationship between the amount of F and any cations, nor did F concentration vary across the grain (table 3).

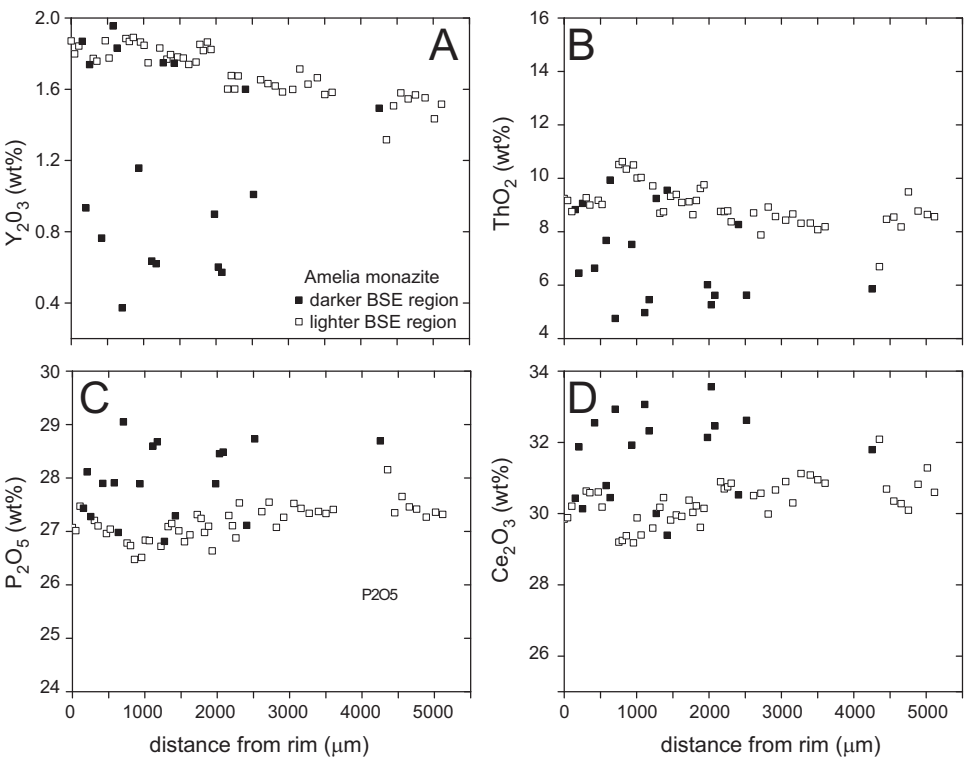

Fig. 7. Transect in EPMA compositions of (A) Y_2O_3 (wt.%), (B) ThO_2 (wt.%), (C) P_2O_5 (wt.%), and (D) Ce_2O_3 (wt.%) across the Amelia monazite grain. Transect begins at rim point 1 in figure 2.

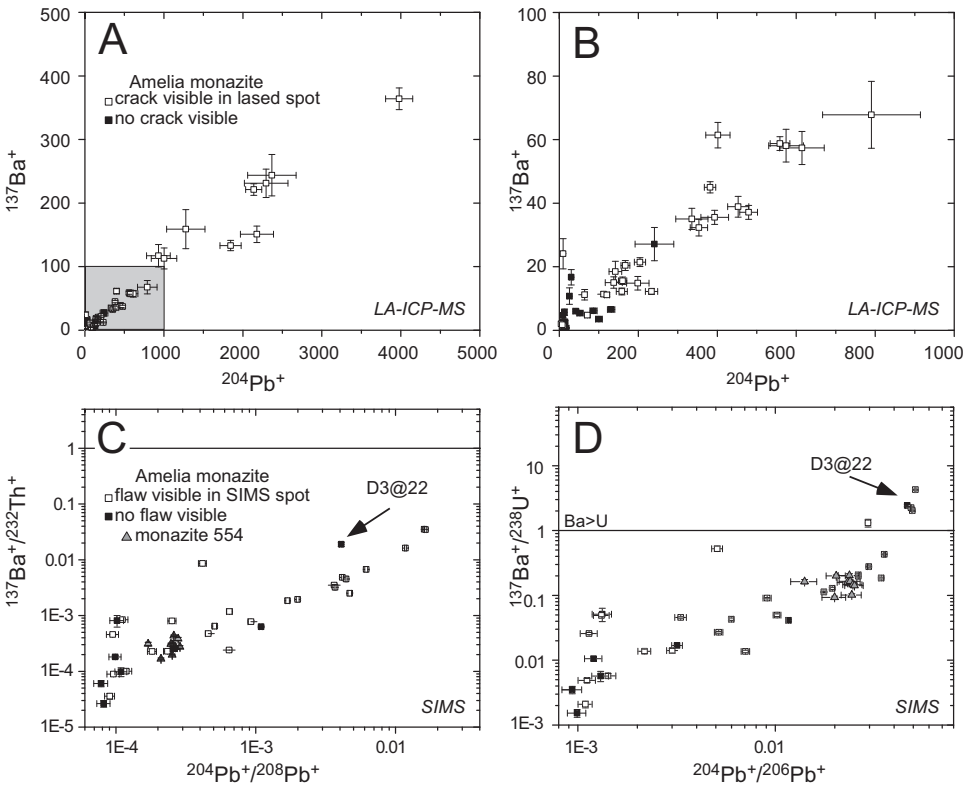

Fig. 8. (A) and (B) Plots of $^{204}Pb^+$ vs. $^{137}Ba^+$ (peak intensities) for the Amelia monazite obtained using LA-ICP-MS. The gray square in panel (A) indicates the area covered in (B). The data fit the equation Ba (ppm) = 0.086±0.004 * ^{204}Pb(ppm) - 0.414±0.124, with r^2 = 0.88. White boxes indicate the spot overlaps cracked region on the monazite, whereas black boxes indicate the spot was placed on a region of the grain where no or smaller (<5 μm in width) microcracks are visible. Plots of (C) $^{204}Pb^+/^{208}Pb^+$ vs. $^{137}Ba^+/^{232}Th^+$ and (D) $^{204}Pb^+/^{206}Pb^+$ vs. $^{137}Ba^+/^{238}U^+$ obtained from spots on the Amelia monazite and monazite 554 using SIMS. A line is drawn where $^{137}Ba^+ = {}^{232}Th^+$ and where $^{137}Ba+ = {}^{238}U^+$. Spots on the Amelia monazite are differentiated if located on a flaw (microcrack, inclusion, or darker BSE region). SIMS spot D3@22 is identified.

The LA-ICP-MS spot transect closely paralleled the EPMA path across the monazite grain (fig. 2). Ablation spots within dark BSE zones associated with microcracks have significantly higher Al, Fe, Ba, and Pb concentrations (intensities) and lower Y and U concentrations compared to regions lacking obvious alteration textures (table 4). Middle and heavy REE (MREE, HREE), Na, Mn, and As show no spatial variation across the grain. SEM reimaging reveal haloes around ablation craters and spherical material within proximal microcracks, consistent with ablation plume ejecta (fig. 5).

We observe a positive correlation (r^2 = 0.88) between common Pb ($^{204}Pb^+$) and Ba ($^{137}Ba^+$), with highest concentrations measured for ablations in proximity to microcracks and lowest concentrations for ablations within areas free from obvious surface irregularities (figs. 8A–8B). Positive correlations also exists for Ba and Al (fig. 9A), indicating that common Pb is enriched in proximity to microfracture networks. Some spots intersecting microcracks have elevated Al + Ba and ^{204}Pb + ^{208}Pb (Pb_{total}) + MREE + HREE contents (figs. 9B and 9C). Figure 9C shows Al + Ba enrichment is particularly related to Pb_{total} + Eu. The elements Y, Th, and U fail to show this relationship with Al + Ba. A trend of increasing Th/U with decreasing Y is

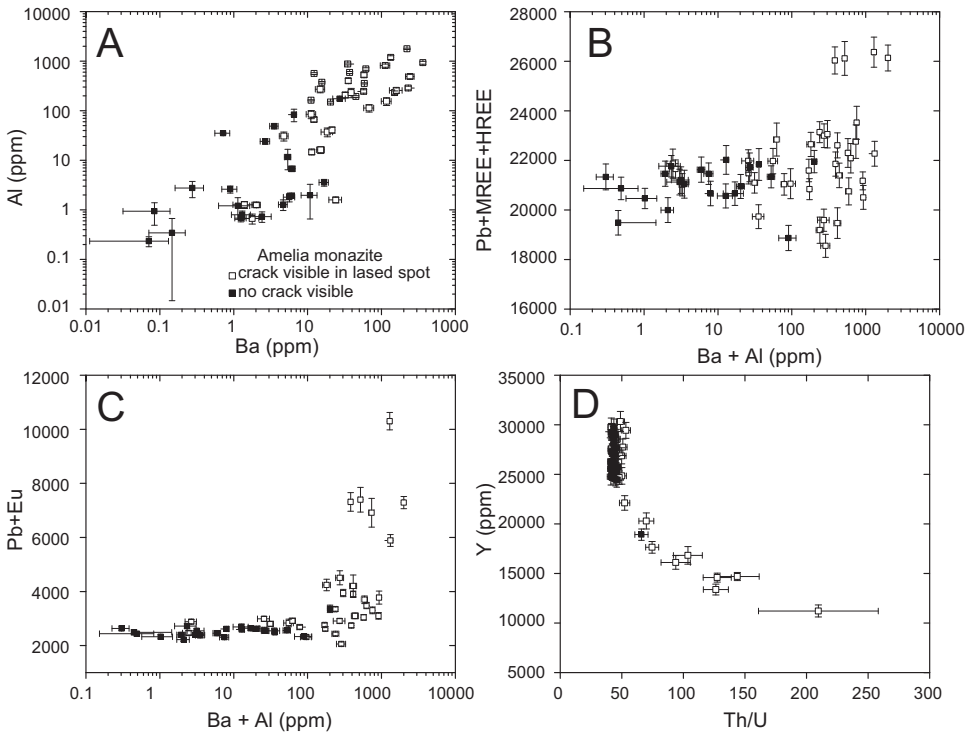

Fig. 9. (A) Ba (ppm) vs. Al (ppm), (B) Ba + Al (ppm) vs. ^{204}Pb + ^{208}Pb + MREE + HREE (ppm), (C) Ba + Al (ppm) vs. ^{204}Pb + ^{208}Pb + Eu (ppm), and (D) Th (ppm)/U (ppm) vs. Y (ppm) for the Amelia monazite grain. Data obtained using LA-ICP-MS. White boxes indicate the spot overlaps cracked region on the monazite, whereas black boxes indicate the spot was placed on a region of the grain where no or smaller (<5 μm in width) microcracks are visible.

observed for some spots overlapping microcracks only (fig. 9D). SE images of these regions in the Amelia monazite have textures consistent with melting in the ablated area with microcracks (fig. 5). The ^{204}Pb peak has several possible, although likely improbable, Ba-related interferences (table 8) unable to be resolved using LA-ICP-MS without a collision/reaction cell, but have the potential to control to the trend seen in figures 8A and 8B.

Amelia monazite ablations have consistent overall REE patterns regardless of whether regions with microcracks or alteration textures were analyzed (fig. 10). The Amelia monazite is LREE enriched with $Ce_N > La_N$. Only some EPMA analyses have negative Eu anomalies, likely the result of approaching the calculated EPMA detection limit of ~0.09 weight percent Eu_2O_3 (average ~0.11±0.05 wt.%, table 3). LA-ICP-MS analyses, however, have pronounced negative Eu anomalies for all spots. Some cracked regions of the grain also contain lower HREE contents.

Ion Microprobe (SIMS) Analysis

Tables 5 and 6 report Amelia monazite Th-Pb ages obtained using the monazite 554 reference age (45 Ma; Force, 1997; Harrison and others, 1999) for each analytical day (n = 3). The data are further sorted by %^{208}Pb* (% radiogenic ^{208}Pb) and spot location. In this regard, we find all spots with ^{208}Pb* < 99 percent are found on regions associated with darker BSE, microcracks, or pits (fig. 3; table 6). For all spots, regardless of location, we obtain an overall average ^{232}Th-^{208}Pb age for the Amelia

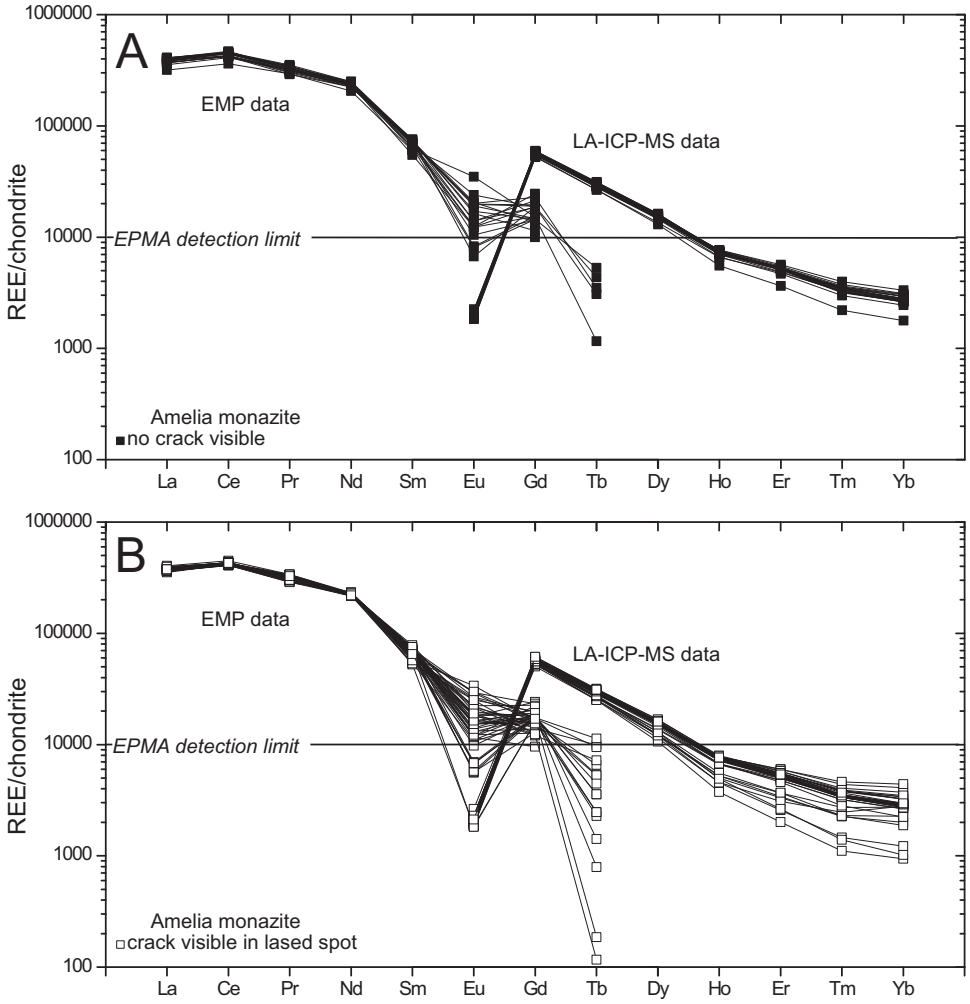

Fig. 10. Chondrite-normalized (Sun and McDonough, 1989) patterns for the Amelia monazite obtained using EPMA and LA-ICP-MS data. The line indicates EPMA detection limits. Panel (A) are patterns for EPMA analyses placed on areas of lighter BSE and LA-ICP-MS data for regions where no crack is visible in the lased spot. Panel (B) shows patterns of EPMA analyses placed on darker BSE regions and LA-ICP-MS data for spots where microcracks are visible.

monazite of 241.0±9.1 Ma (±1σ; weighted mean age 242.6±0.7 Ma, MSWD = 10.3; n = 59 spots). Ages from spots with ^{208}Pb* > 99 percent, regardless of location (n = 24) range from 277.6±4.9 Ma to 227.0±7.2 Ma. Culling these to spots from polished regions of the grain free from visible flaws yields a similar range (261.8±5.5 Ma to 229.0±6.8 Ma, n = 8; table 5). Spots with ^{208}Pb* < 99 percent (n = 35) yield a wider age range from 332.1±12.7 Ma to 196.0±5.4 Ma. The oldest age is located on a spot that intersects a small darker zone in BSE (fig. 3F) and the youngest age is located on a set microcracks and darker region in BSE (fig. 3C). Although visibly altered portions of the grains have ^{208}Pb* < 99 percent, Ba contents may also flag altered grain regions with higher radiogenic Pb contents. In this regard, the spot with ^{208}Pb* > 99 percent and high $^{137}Ba^{+}/Th^{+}$ (8.11) is located on a darker region in BSE (fig. 3B).

Using SIMS, both the Amelia monazite and the standard monazite 554 show correlations between radiogenic Pb contents and $^{137}Ba^+/Th^+$ or $^{137}Ba/U^+$ (figs. 8C and 8D), indicating the LA-ICP-MS trend seen in figures 8A and 8B represents the covariation of Ba with ^{204}Pb, rather than with a Ba-related polyatomic interference on m/z 204. Operating the ion microprobe with a MRP of 5000 (vs. ~300 for LA-ICP-MS) is sufficient to exclude Ba-related (^{136}Ba, ^{137}Ba, and ^{138}Ba) polyatomic interferences on ^{204}Pb (table 8). The Amelia monazite defines linear trends in plots of $^{137}Ba^+/Th^+$ vs. $^{204}Pb^+/^{208}Pb^+$ ($r^2 = 0.73$) and $^{137}Ba/U^+$ vs. $^{204}Pb^+/^{206}Pb^+$ ($r^2 = 0.59$). Analyses of the highly radiogenic standard grain monazite 554 has $^{137}Ba^+/Th^+$ of $2.93 \times 10^{-4} \pm 1.58 \times 10^{-5}$ and $^{137}Ba/U^+$ of 0.15 ± 0.01. These values lie within the trend defined by the Amelia monazite data in $^{137}Ba^+/Th^+$ or $^{137}Ba^+/U^+$ vs. $^{204}Pb^+/^{208}Pb^+$ plots (figs. 8C and 8D). Spots with higher $^{137}Ba^+/Th^+$ (>0.0003) are commonly associated with analyses that overlap flaws (figs. 3, 8C and 8D). Spot D3@22, which is located on a region free from flaws (fig. 3E), is a notable exception to this observation. This spot is one of only five measurements with $^{137}Ba^+/U^+ > 1$ (fig. 8D). All analyses with $^{137}Ba^+/U^+ > 1$ have higher common Pb contents and are located on darker BSE regions (spots D3@4a, D3@13, D3@14, D3@20, and D3@22, fig. 3). Most of these yield younger ages compared to spot locations free from secondary alteration features (table 6).

The population of ages for spots with $^{208}Pb^* > 99\%$ is bimodal, with peaks centered at 263.5±3.0 Ma (±1σ; MSWD = 1.7; n = 11) and 234.1±3.6 Ma (±1σ; MSWD = 0.4; n = 13) (fig. 11A) and a lack of intermediate ages within the 250±4 Ma time frame. The bimodal distribution remains when all of the data are plotted, regardless of ^{208}Pb content (fig. 11B).

DISCUSSION AND CONCLUSIONS

Amelia Monazite Chemistry

The geochemistry and ages of distinct regions in the Amelia monazite grain provide insight into the processes that affected the greater pegmatite system following crystallization. Yttrium, HREEs, and F may trace reactions that modify monazite compositions (Heinrich and others, 1997; Zhou and others, 2008; Krenn and Finger, 2010; Spear and Pyle, 2010; Didier and others, 2013; Kylander-Clark and others, 2013). Here we suggest Ba can trace common Pb addition within areas in monazite affected by secondary alteration. To our knowledge, hollandite [$Ba(Mn_6Mn_2)O_{16}$] is the only Ba-phase reported for the Morefield Mine pegmatite (Kearns and Martin, 2000). We found no trace of Mn using EPMA (table 3) and only 12.0±3.6 ppm Mn using LA-ICP-MS (table 4). Depending on its specific composition, detector gain and signal offset, barite ($BaSO_4$) would appear slightly darker or indistinguishable from monazite in BSE based on its average atomic number. The only bright phase within the cracks in the grain we observed is thorite (figs. 2 and 3). Microcracks and their proximal zones are darker regions in BSE (figs. 2 and 3).

The Amelia monazite grain experienced localized alteration as evidenced by recrystallization along microcracks and within the grain itself (figs. 2 and 3). Such secondary processes are expected, considering the Morefield Mine pegmatite was emplaced along fractures and developed in a magmatic phases followed by significant hydrothermal alteration (Lemke and others, 1953; Kearns, 1995; Smerekanicz and Dudas, 1999). Regions of the monazite grain surface characterized by darker BSE contrast (fig. 3) have stoichiometry consistent with the ideal monazite formula (fig. 4) and are concentrated in microcracked regions that cross cut primary monazite zoning, which indicate the grain was affected secondary alteration. At least two generations of darker monazite are present (fig. 3). The chemistry of these regions vary, and ranges from 9.55 to 4.75 weight percent ThO_2 and 0.56 to 1.96 weight percent Y_2O_3. Some

darker BSE regions are lower in Y compared to lighter regions of the grain (fig. 7A; tables 3 and 4).

Yttrium is often used to trace the monazite reaction history in metamorphic assemblages that contain xenotime and/or garnet, and higher amounts of Y in monazite in metamorphic rocks have been linked to increasing grade (Heinrich and others, 1997; Zhu and Onions, 1999; Mahan and others, 2006; Zhou and others, 2008; Krenn and Finger, 2010; Spear and Pyle, 2010). Although the Amelia monazite formed initially in a pegmatite with several Y-bearing species (allanite, fergusonite, fersmite; Lumpkin, 1988), recrystallized zones contain lower Y, lower Th, and higher REE (fig. 7). These areas may have formed post-crystallization during fracturing under lower-grade conditions compared to monazite that crystallized during primary emplacement. The darker BSE regions correspond to secondary zones that formed via dissolution and reprecipitation along microcracks in the lighter BSE domains. Thorium contents decreased (~2 wt. %) in altered monazite areas, possibly synchronous with localized thorite formation. Regions of darker BSE in the Amelia monazite average 7.04±1.68 weight percent ThO_2, whereas lighter BSE average 8.98±0.75 weight percent (table 3).

HREE distributions (defined as Tb, Dy, Ho, Er, Yb, Lu, table 4) are increasingly being used to interrogate monazite ages (Kylander-Clark and Hacker, 2011; Cottle and others, 2012; Baldwin and others, 2013; Holder, and others, 2013; Kylander-Clark and others, 2013; Stevens and Baldwin, 2013). Like Y, HREE distribution in monazite is linked to reactions with garnet or xenotime in metamorphic assemblages and migmatites (Kylander-Clark and others, 2013; Broussolle and others, 2015). Owing to concentrations near or below EPMA detection limits, LA-ICP-MS provides more reliable HREE concentrations. Overall, HREE contents for lighter and darker BSE regions of the Amelia monazite show little statistical difference (table 4). Some regions with microcracks have lower HREE/chondrite compared to those where no crack was visible, but many patterns overlap (fig. 10). Although material proximal to and filling microcracks are affected by secondary dissolution and reprecipitation, the hydrothermal fluids associated with monazite alteration may have been buffered with respect to REE, such that altered areas fail to show systematic differences in HREE contents. The melt-fluid system in which the Morefield Mine pegmatite formed is thought to have been initially enriched in REE (Lumpkin, 1998). Overall, EPMA analyses of the darker BSE regions in the Amelia monazite have higher LREE (La, Ce, Pr, and Nd, table 3; also fig. 7D).

Fluorine-rich fluids are an effective medium for transporting Y and REE in a variety of geologic environments (Keppler, 1993; Hetherington and Harlov, 2008; Sheard and others, 2012; Papoutsa and Pe-Piper, 2013; Tropper and others, 2013). These fluids appear to enhance the mobility of Th compared to U and may contribute common Pb to monazite (Didier and others, 2013). Elevated F contents are reported in monazite affected by secondary fluid-mediated alteration (0.3–0.6 wt. %; Hetherington and Harlov, 2008) and metal ore deposits (0.48±0.07 wt. %; Sheard and others, 2012). EPMA and LA-ICP-MS analyses of the Amelia monazite show no spatial relationship exists between F and common Pb, and F contents are similar across the grain (table 3).

Both LA-ICP-MS and SIMS data demonstrate a clear positive correlation between common Pb (^{204}Pb) and ^{137}Ba in altered regions of the Amelia monazite (fig. 8). If resident within the primary monazite composition, Pb^{2+} and Ba^{2+} would reside in a 9-fold coordination site due to their similar ionic radii (1.35Å and 1.47Å, respectively; Shannon 1976; Ni and others, 1995). Barium in monazite has been reported (Masuda and Nakai, 1983; de Toledo and Pereira, 2003; McFarlane and McCulloch, 2007; Buick and others, 2011) and is stable in its structure despite its larger radius compared to

other elements that typically reside in the 9-fold coordination site (Montel and others, 2002; Clavier and others, 2011). In a study of the synthesis of $BaTh(PO_4)_2$, the monazite structure was achieved at 2.5kbar and 700 °C (Montel and others, 2002), P-T conditions the Morefield Mine pegmatite could have reasonably experienced based on its composition (London, 2005). Barium may also enter the monazite structure via the decay of ^{138}La (to ^{138}Ba, Masuda and Nakai, 1983; Nakai and others, 1986), but this is not a significant Ba source due to the low natural abundance of ^{138}La (0.09% compared to 99.910% ^{137}La) and extremely long half-life (210 Ga, Dickin, 1987). We also find no statistical difference in La_2O_3 contents between the lighter and darker BSE regions (10.45±0.33 wt. % vs, 10.79±0.44 wt. %, table 3). Thus, the source of Ba correlated with common Pb seems likely to be allogenic.

The presence of an alteration product is a viable alternative explanation for the higher concentrations of Ba and Pb found in microcrack regions of the Amelia monazite. Ba-bearing alteration products in association with microcracks could include gorceixite [$(BaAl_3(PO_4)(PO_3OH)(OH)_6$] and Ba-rich plumbogummite [$PbAl_3(PO_4)_2(OH)_5{\cdot}H_2O$]. Trace amounts of such phases could explain the positive associations of Ba, Al and common Pb documented in microcrack-proximal areas of the grain (fig. 8). This hypothesis is supported by significantly higher ^{27}Al contents associated with microcracks versus non-altered regions using LA-ICP-MS (221±28 ppm vs. 18.5±19.2 ppm; table 4). Gorceixite is rare, but can found in carbonatite complexes (de Toledo and Pereira, 2003), "unusual" granitic assemblages (Petrik and others, 2011), and in REE-bearing pegmatites due to reactions associated with post-magmatic fluid activity (Baldwin and others, 2000). Several studies report monazite-gorceixite associations (Sweatman, ms, 1961; Staatz and others, 1979; Michel and others, 1982; Rasmussen, 1996; van Hees and others, 2002). Lead can substitute for Ba in gorceixite (Milton and others, 1958; Taylor and others, 1984). Monazite has also been found in association with plumbogummite in quartz-apatite veins associated with uranium-rich granites (Rojkovic and others, 1999), mining tailings (Rollinson and others, 2007) and soils (Qureshi and others, 1969).

The link between Ba and ^{204}Pb cannot be explained via an external contaminant related to sample preparation. Alumina introduced in the microcracks during polishing is unlikely because we consistently and extensively cleaned the sample to remove any polishing compound and pre-ablated sample spots prior to LA-ICP-MS analysis. Hollandite and barite are other Ba-bearing phases that could host common Pb. Hollandite is unlikely because as Mn does not trend with ^{204}Pb nor increases in concentration in microcracks. Barite was not observed.

Amelia Monazite Ages: Tectonic Interpretation

Our average ^{232}Th-^{208}Pb age for all Amelia monazite SIMS analyses (241.0±9.1 Ma) overlaps with previously reported whole grain ^{268}U-^{206}Pb ID-TIMS and ^{232}Th-^{208}Pb LA-ICP-MS, Amelia monazite ages and a K-Ar muscovite age for the Morefield Mine pegmatite (table 1). The overall distribution of ^{232}Th-^{208}Pb ages ranges over a ~136 million year interval, from Mississippian to Late Jurassic, depending on spot location (tables 5 and 6). Such a wide spread of ages is not unexpected considering the complexity of secondary alteration features throughout the grain (figs. 2 and 3), the multi-stage tectonic evolution of the region (Smerekanicz and Dudas, 1999), and the diversity of ages previously derived for the Amelia monazite and associated minerals (table 1). Indeed, monazite ages in pegmatites may record different stages of crystallization or isotopic re-equilibration during tectonothermal events (Viana and others, 2003; Lupulescu and others, 2011; McCauley and Bradley, 2014). When we restrict the ages to spots with highest radiogenic Pb contents (>99% ^{208}Pb*), a bimodal distribution is revealed (fig. 11A), with peaks centered at 263.5±3.0 Ma ("Mid" Permian) and 234.1±3.6 Ma (Late Triassic). Peterman and others (2012)

previously reported Permian ages for the Amelia monazite, but these are first documented Triassic results <240 Ma.

The age distributions obtained for each of the three days indicate we targeted younger, more radiogenic age domains on Day 3 compared to the other days (tables 5 and 6). If the bimodal age distribution for spots with >99 percent ^{208}Pb* results from analytical bias during the SIMS sessions, this would be identified by the monazite 554 age standard. However, table 7 shows the standard age was reproduced on all three days within the expected level of precision. In addition, if the younger age trend on Day 3 is related to instrument problem, we should observe significantly different monazite standard calibration slopes and intercepts on Day 1 compared to Day 3 for spots with highly radiogenic ^{208}Pb* only; values required to shift these particular ages by 20 to 30 myrs. Comparing the calibrations for these days only, we see similar slopes, intercepts, and ranges of ThO_2^+/Th^+ (from 3.892±0.018 to 4.353±0.008 for Day 1 and from 3.455±0.021 to 4.774±0.022 for Day 3) (table 7). All data regardless of radiogenic Pb content show no preferred age distribution based on day the analysis was obtained. Overall, ages range from 198.6±30.1 Ma (15.0±1.6% ^{208}Pb*) to 281.9±4.2 Ma (97.0±0.05% ^{208}Pb*) on Day 1 to 196.0±5.4 Ma (38.5±0.3% ^{208}Pb*) to 268.1±5.6 Ma (99.7±0.02% ^{208}Pb*) on Day 3 (tables 5 and 6). If we broaden the age distribution to include spots with <99 percent ^{208}Pb*, we find a similar spread of ages (differing by 70–115 Ma) was obtained on each of the analytical days (tables 5 and 6) and a similar bimodal distribution appears (fig. 11B).

Although we consider ages for spots with >99 percent ^{208}Pb* to best record tectonothermal episodes affecting Amelia monazite composition (table 5), it is perplexing that the bimodal age distributions fail to clearly correspond to regions within the grain such as visual contrasts with associated chemical attributes (fig. 3). The possibility we sampled a region that differs from our interpretations (altered vs. least-altered, tables 5 and 6) is remote because we imaged the grain surface before and after analyses. Correlations between monazite age and composition do not always exist (Hokada and Motoyoshi, 2006; Hinchey and others, 2007; Martin and others, 2007; Triantafyllidis and others, 2010; Reno and others, 2012; see review in Catlos, 2013), and our visual observations are mainly restricted to monazite appearance using BSE only. Regions with darker BSE contrast occur within and in close proximity to microcrack networks and appear to crosscut zones of interpreted primary sector growth (figs. 2 and 3D, 3F, 3H), textural attributes similar to monazite that has undergone dissolution and reprecipitation (Seydoux-Guillaume and others, 2012). Most of the localities where SIMS analyses yield <99 percent ^{208}Pb* and ages younger than 263.5±3.0 Ma are located on darker regions in BSE (table 6). Considering the bimodal age distribution, these results suggest the timing of some secondary monazite growth may overlap within uncertainty with primary crystallization. In subsequent tectonic interpretations, we consider the two statistically significant age peaks corresponding to SIMS localities with >99 percent ^{208}Pb* (fig. 12, table 5).

Our preferred Amelia monazite crystallization age (263.5±3.0 Ma, Middle Permian) is consistent with some of the youngest reported Appalachian pegmatite bodies (Pulver and others, 1997; Robinson and others, 2007; Walsh and others, 2007a, 2007b; Gibson and others, 2011; Kunk and others, 2011; Bradley and others, 2013). These are interpreted as late stage intrusives associated with terminal (Permian) Alleghanian convergence between Laurentia and Africa (Hatcher, 2010). These pegmatites may have been emplaced as late as 275 Ma (Walsh and others, 2007b) or between 270 to 250 Ma (Robinson and others, 2007). Our prospective Amelia monazite crystallization age thus may have formed during or 10 myrs after the final large-scale docking of west Africa.

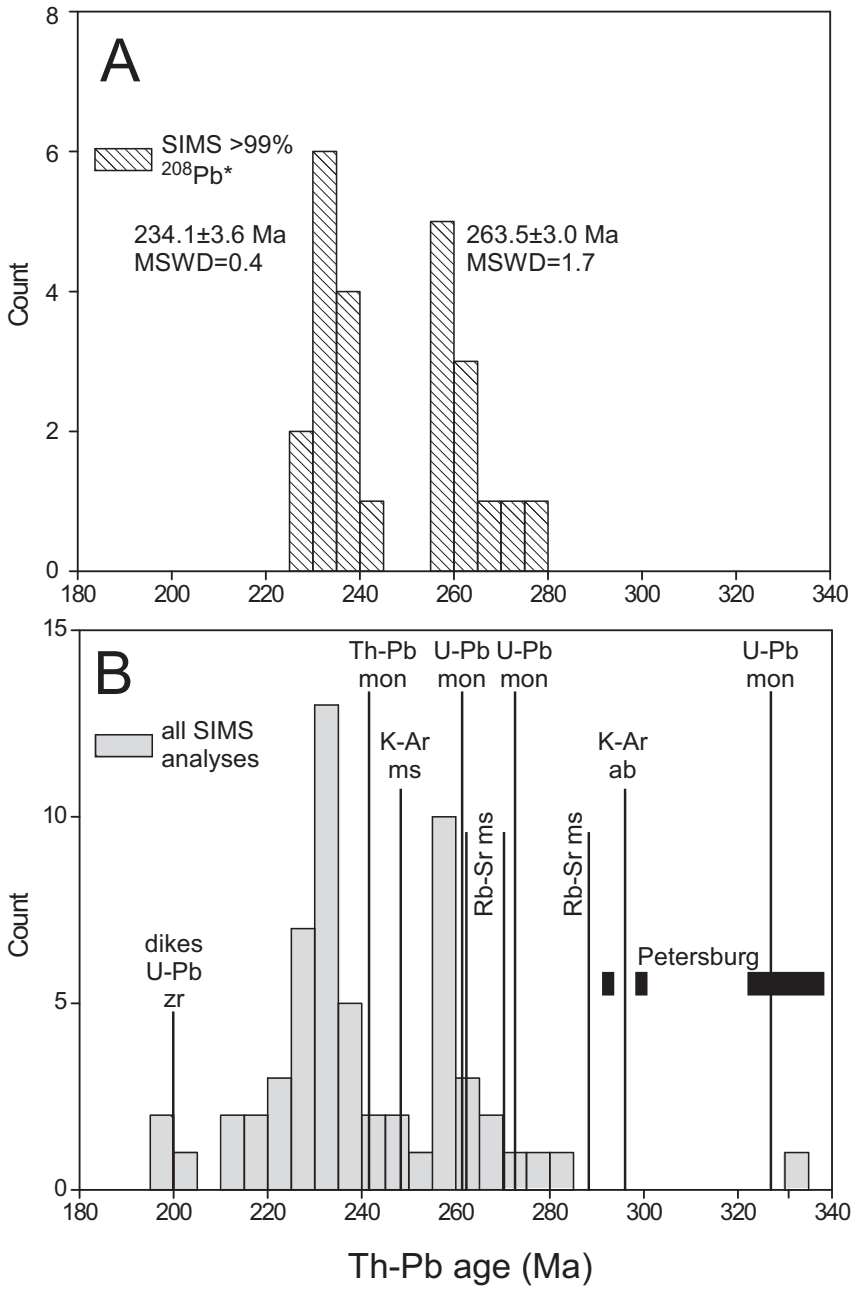

Fig. 11. Histograms of ^{232}Th-^{208}Pb SIMS ages from the Amelia monazite. See tables 5 and 6 for analytical data. Panel (A) reports ages with only >99% radiogenic ^{208}Pb*. Panel (B) includes all of the data with Amelia monazite ages (table 1) indicated by lines. Horizontal black boxes represent ages from the Petersburg granite.

The bimodal Amelia monazite ages presented here are younger than those available for surrounding granitic intrusions (fig. 1, table 1). However, documentation of age control for most of these plutons (Columbia, Red Oak, Buggs Island, and Burkeville) is limited to abstracts and conference proceedings from which it is difficult or impossible to evaluate the quality of the age determination.

A single Amelia monazite spot yielded an age (D2@34: 332.1±12.7 Ma, fig. 3F; ^{208}Pb* = 98.1%; table 6) overlaps with the Petersburg granite (330±8 Ma to 296.33±0.11 Ma, Carter, 2011, table 1). This pluton was initially mapped as a two-feldspar muscovite-biotite granite with a poorly to moderately developed tectonic foliation (Bobyarchick and Glover, 1979), but Carter (2011) document a more complex assembly of at least five units (granite gneiss, foliated, megacrystic, porphyritic, and subidiomorphic granite bodies). However, as this Amelia monazite age has a larger uncertainty than is typical for SIMS analyses, derives from an altered region of the grain, and no similar ages were derived on other spots, we did not consider it for interpretations.

Activity along the Hylas Fault (fig. 1) (Weems, ms, 1974; Gates and Glover, 1989) is constrained by ages reported from the Petersburg granite listed in table 1, as the structure accommodated repeated pulses of magma emplacement (Buchwaldt and Owens, 2012). The NE-striking Hylas Fault is one of the easternmost Alleghanian shear zones that accommodated dextral strike-slip motion (Bobyarchick and Glover, 1979; Gundersen and Gates, 1995). This type of activity, where magma uses releasing offsets in fault structures as emplacement conduits, is also proposed for the Buggs Island granite that intrudes the Nutbrush Creek Fault Zone located ~40 km south of the Morefield Mine pegmatite (fig. 1) (Butler and Horton, 1995). The Hylas and Nutbrush Creek fault zones are physically connected by the Lake Gordon mylonite zone (Horton and others, 1993; Blake and Stoddard, 2011), which is loosely constrained to be Late Paleozoic based on its tectonic relationship constraining magma emplacement associated with the Buggs Island pluton (Horton and others, 1993; Sacks, 1999). Gundersen and Gates (1995) speculate the Morefield Mine pegmatite emplacement corresponds to an earlier (pre-Alleghanian) interval of movement along the Hylas Fault, but this interpretation is inconsistent with the monazite ages reported here. The Morefield Mine pegmatite is located ~40 km west of the Spotsylvania lineament or high strain zone (fig. 1) (Nueschel, 1970; Bailey, 2004; Spears and others, 2004), but this structure also pre-dates the pegmatite (Wortman and others, 1998; Hibbard, 2000).

Based on ^{40}Ar/^{39}Ar hornblende ages from regionally metamorphosed amphibolite assemblages, the Hylas Fault experienced a brittle-ductile transition by ~262 Ma (Durrant and others, 1980; Gates and Glover, 1989). This transition represents either a large-scale switch in plate motion as the fault changed from transpression to transtension, or extensional overprinting on an older Paleozoic transpressional regime (Blake and others, 2001). The timing of the transition overlaps with the prospective 263.5±3.0 Ma crystallization age of the Amelia monazite, leaving open the possibility that the Hylas Fault operated as a fluid migration system from the Petersburg granite to the Morefield Mine pegmatite. If so, a magmastatic gradient (a lower hydraulic head) related to fracturing and fracture dilation along Hylas Fault segments may have tapped Petersburg melts, which evolved and ultimately intruded the Maidens Gneiss as the Morefield Mine pegmatite (for example, Lambert and others, 2013). Based on ^{40}Ar/^{39}Ar ages of biotite and hornblende, the Maidens Gneiss experienced syntectonic cooling between 280 Ma and 260 Ma, within this time frame (Durrant and others, 1980; Smerekanicz and Dudas, 1999). Pegmatite formation associated with such transcurrent tectonic settings is widely reported around the world (Nova Scotia - Murphy and others, 1998; Central Appalachians - Gates and others, 2007; Namibia, South Africa - Lambert and others, 2013; Nigeria - Okunlola, 2013; Brazil -Sallet and others, 2015).

Although dextral faulting along the Hylas Fault ended prior to 241 Ma (Gates and Glover, 1989), the structure records a subsequent Triassic (~220 Ma) episode of high-angle normal faulting and brittle activity (Bobyarchick and Glover, 1979; Hollis and Bailey, 2012; Horton and others, 2014). Lutz and Venkatakrishnan (1985) suggest sinistral strike-slip movement occurred during the Triassic based on deformed diabase dikes along the Hylas Fault. The younger bimodal age recorded by the Amelia monazite (234.1±3.6 Ma), derived substantially from altered spot localities (tables 5 and 6) could thus be consistent with Triassic normal or possible sinistral faulting linked to lower temperature development and deformation of local rift basins (Venkatakrishnan, 1987; Venkatakrishnan and Watkins, 1988).

ACKNOWLEDGMENTS

We thank Matt Kohn (Boise State University) for supplying the monazite grain analyzed in this study and Isis Gaber (UT Austin) for sample preparation. We appreciate analytical assistance and discussions with George Morgan at the University of Oklahoma Electron Microprobe Laboratory, and Patrick Smith at the Jackson School of Geosciences Bureau of Economic Geology electron microbeam facility, Axel Schmitt and Rita Economos from UCLA SIMS facility. We appreciate discussions with Alfredo Petrov about the geochemical results. The ion microprobe facility at UCLA is partly supported by a grant from the Instrumentation and Facilities Program, Division of Earth Sciences, National Science Foundation. We appreciate constructive comments from an anonymous reviewer, Brent Owens, and Paul Tomascak.

SUPPLEMENTARY DATA

Excel Spreadsheet data. EPMA and LA-ICP-MS are provided. http://earth.geology.yale.edu/%7eajs/SupplementaryData/2016/01Catlos.xlsx.

REFERENCES

Aleinikoff, J. N., Hayes, T. S., Evans, K. V., Mazdab, F. K., Pillers, R. M., and Fanning, C. M., 2012, SHRIMP U/Pb Ages of xenotime and monazite from the Spar Lake Red Bed-associated CU–Ag Deposit, Western Montana: Implications for ore genesis: Economic Geology, v. 107, n. 6, p. 1251–1274, http://dx.doi.org/10.2113/econgeo.107.6.1251

Bailey, C. M., 2004, Significant southwestward transport of the Goochland Terrane along the Spotsylvania high-strain zone, Virginia Piedmont: Geological Society of America Abstracts with Programs, v. 36, n. 2, p. 106.

Bailey, C. M., and Owens, B. E., 2012, Traversing suspect terranes in the central Virginia Piedmont: From Proterozoic anorthosites to modern earthquakes: Geological Society of America Field Guide, v. 29, p. 327–344, http://dx.doi.org/10.1130/2012.0029(10)

Bailey, C. M., Owens, B. E., and Shirvell, C. R., 2005, Northern ancestry for the Goochland terrane as a displaced fragment of Laurentia: Comment and Reply: COMMENT: Geology, v. 33, n. 1, p. e70, http://dx.doi.org/10.1130/0091-7613-33.1.e70

Baldwin, J. A., Guevara, V. E., and Foster, D. A., 2013, Constraining the Proterozoic growth and modification of the western North American Craton in northern Idaho using monazite and xenotime petrochronology: Geological Society of America Abstracts with Programs, v. 45, n. 7, p. 880.

Baldwin, J. R., Hill, P. G., von Knorring, O. O., and Oliver, G. J. H., 2000, Exotic aluminum phosphates, natromontebrasite, brazilianite, goyazite, gorceixite and crandallite from rare-element pegmatites in Namibia: Mineralogical Magazine, v. 64, n. 6, p. 1147–1164, http://dx.doi.org/10.1180/002646100549940

Bartholomew, M. J., and Tollo, R. P., 2004, Northern ancestry for the Goochland Terrane as a displaced fragment of Laurentia: Geology, v. 32, n. 8, p. 669–672, http://dx.doi.org/10.1130/G20520.1

Blake, D. E., and Stoddard, E.F., 2011, Transcurrent transfer zone and dextral releasing offset; the Nutbush Creek-Lake Gordon Fault system in the eastern North Carolina Piedmont: Geological Society of America Abstracts with Programs, v. 43, n, 2, p. 16.

Blake, D. E., Clark, T. W., Stoddard, E. F., Hames, W. E., Heller, M. J., Grimes, W. S., Robitaille, K. R., and Hibbard, J. P., 2001, Ductile-brittle relationships on the western flank of the Raleigh metamorphic belt, North Carolina: Geological Society of America Abstracts with Programs, v. 33, n. 2, p. 19.

Bobyarchick, A. R., and Glover, L., III, 1979, Deformation and metamorphism in the Hylas Zone and adjacent parts of the eastern Piedmont in Virginia: Geological Society of America Bulletin, v. 90, n. 8, p. 739–752, http://dx.doi.org/10.1130/0016-7606(1979)90<739:DAMITH>2.0.CO;2

Boggs, K. J. E., Kamo, S. L., Simony, P. Moore, J., and Archibald, D., 2002, A comparison of CHIME and

ID-TIMS U/Pb monazite ages from the Rocky Mountain Trench near Golden, British Columbia, Canada and the importance of CHIME analyses: Geological Society of America Abstracts with Programs, v. 34, p. 68.

Bradley, D., Buchwaldt, R., Shea, E., Bowring, S., O'Sullivan, P., Benowitz, J., and Bradley, L., 2013, Geochronology and orogenic context of Northern Appalachian lithium-cesium-tantalum pegmatites: Geological Society of America Abstracts with Programs, v. 45, n. 1, p. 108.

Broussolle, A., Stipska, P., Lehmann, J., Schulmann, K., Hacker, B. R., Holder, R., Kylander-Clark, A. R. C., Hanzel, P., Racek, M., Hasalová, P., Lexa, O., Hrdlickova, K., and Burianek, D., 2015, *P-T-t-D* record of crustal-scale horizontal flow and magma-assisted doming in the SW Mongolian Altai: Journal of Metamorphic Geology, v. 33, n. 4, p. 359–383, http://dx.doi.org/10.1111/jmg.12124

Buchwaldt, R., and Owens, B., 2012, Decoding the multiscale magmatic cyclicity of magmatic pluton constructions using the Petersburg Granite, Virginia, USA, as an example: Geological Society of America Abstracts with Programs, v. 44, n. 7, p. 498.

Buick, I. S., Lana, C., and Gregory, C., 2011, A LA-ICP-MS and SHRIMP U/Pb age constraint on the timing of REE mineralisation associated with Bushveld granites: South African Journal of Geology, v. 114, n. 1, p. 1–14, http://dx.doi.org/10.2113/gssajg.114.1.1

Burt, D. M., 1989, Compositional and phase relations among rare earth element minerals: Reviews in Mineralogy and Geochemistry, v. 21, p. 259–307.

Butler, J, and Horton, J., 1995, The Buggs Island granite pluton, emplacement related to right-lateral faulting in the eastern Piedmont, Virginia and North Carolina. Geological Society of America Abstracts with Programs, v. 27, n. 2, p. 39.

Carter, M. W., 2011, Subdivisions and field relations in the composite Petersburg Batholith near Richmond, VA: Geological Society of America Abstracts with Programs, v. 43, n. 2, p. 16.

Catlos, E. J., 2013, Versatile monazite: resolving geological records and solving challenges in materials science- Generalizations about monazite: Implications for geochronologic studies: American Mineralogist, v. 98, n. 5–6, p. 819–832, http://dx.doi.org/10.2138/am.2013.4336

Catlos, E. J., and Çemen, I., 2005, Monazite ages and the evolution of the Menderes Massif, western Turkey: International Journal of Earth Sciences, v. 94, n. 2, p. 204–217, http://dx.doi.org/10.1007/s00531-005-0470-7

Catlos, E. J., Gilley, L. D., and Harrison, T. M., 2002, Interpretation of monazite ages obtained via *in situ* analysis: Chemical Geology, v. 188, n. 3–4, p. 193–215, http://dx.doi.org/10.1016/S0009-2541(02)00099-2

Clavier, N., Podor, R., and Dacheux, N., 2011, Crystal chemistry of the monazite structure: Journal of the European Ceramic Society, v. 31, n. 6, p. 941–976, http://dx.doi.org/10.1016/j.jeurceramsoc.2010.12.019

Corfu, F., 1988, Differential response of U–Pb systems in coexisting accessory minerals, Winnipeg River, Canadian Shield: Implications for Archean crustal growth and stabilization: Contributions to Mineralogy and Petrology, v. 98, n. 3, p. 312–325, http://dx.doi.org/10.1007/BF00375182

Cottle, J. M., Kylander-Clark, A., and Hacker, B. R., 2012, Monazite petrochronology by laser ablation split stream inductively coupled plasma mass spectrometry (LASS-ICPMS): Mineralogical Magazine, v. 76, p. 1601.

de Toledo, M. C. M., and Pereira, V. P., 2003, Ocorrência e variabilidade de composição dos fosfatos do grupo da monazita em carbonatitos: Pesquisas em Geociências, v. 30, p. 83–98.

Deuser, W. G., and Herzog, L. F., 1962, Rubidium-strontium age determinations of muscovites and biotites from pegmatites of the Blue Ridge and Piedmont: Journal of Geophysical Research, v. 67, n. 5, p. 1997–2004, http://dx.doi.org/10.1029/JZ067i005p01997

Dickin, A. P., 1987, La-Ce dating of Lewisian granulites to constrain the ^{138}La beta -decay half-life: Nature, v. 325, p. 337–338, http://dx.doi.org/10.1038/325337a0

Dicken, C. L., Nicholson, S. W., Horton, J. D., Kinney, S. A., Gunther, G., Foose, M. P., and Mueller, J. L., 2008, Preliminary integrated geologic map databases for the United States: Delaware, Maryland, New York, Pennsylvania, and Virginia: Open-File Report - U. S. Geological Survey, version 1.1, http://pubs.usgs.gov/of/2005/1325/index.htm.

Didier, A., Bosse, V., Boulvais, P., Bouloton, J., Paquette, J. L., Montel, J. M., and Devidal, J. L., 2013, Disturbance versus preservation of U–Th–Pb ages in monazite during fluid-rock interaction: Textural, chemical and isotopic *in situ* study in microgranites (Velay Dome, France): Contributions to Mineralogy and Petrology, v. 165, p. 1051–1072, http://dx.doi.org/10.1007/s00410-012-0847-0

D'Oriano, C., Da Pelo, S., Podda, F., and Cioni, R., 2008, Laser-ablation inductively coupled plasma mass spectrometry (LA-ICP-MS); setting operating conditions and instrumental performance: Periodico Di Mineralogia, v. 77, p. 65–74.

Druhan, R. M., and Rollins, F. O., 1984, The Nutbush Creek fault zone in the Eastern Piedmont of North Carolina: Geological Society of America Abstracts with Programs, v. 16, p. 135.

Durrant, J. M-, Sutter, J. F., and Glover, L., Ill, 1980, Evidence for an Alleghanian (Hercynian?) metamorphic event in the Piedmont province near Richmond, Virginia: Geological Society of America Abstracts with Programs, v. 12, p. 176.

Farrar, S. S., 1984, The Goochland granulite terrane: Remobilized Grenville basement in the eastern Virginia Piedmont: Geological Society of America Special Paper, v. 194, p. 215–227, http://dx.doi.org/10.1130/spe194-p215

Fontaine, W. F., 1883, Notes on the occurrence of certain minerals in Amelia County, Virginia: American Journal of Science, Series 3, v. 25, n. 149, p. 330–339, http://dx.doi.org/10.2475/ajs.s3-25.149.330

Force, E. R., 1997, Geology and mineral resources of the Santa Catalina Mountains, southeastern Arizona: Tucson, Arizona, Monographs in Mineral Science, Center for Mineral Resources, v. 1, p 1–135.

Fullagar, P. D., 1971, Age and origin of plutonic intrusions in the piedmont of the southeastern Appala-

chians: Geological Society of America Bulletin, v. 82, n. 10, p. 2845–2862, http://dx.doi.org/10.1130/0016-7606(1971)82[2845:AAOOPI]2.0.CO;2

Gates, A. E., and Glover, L. I., 1989, Alleghanian tectono-thermal evolution of the dextral transcurrent Hylas Zone, Virginia Piedmont, U.S.A.: Journal of Structural Geology, v. 11, n. 4, p. 407–419, http://dx.doi.org/10.1016/0191-8141(89)90018-7

Gates, A. E., Valentino, D. W., Gorring, M. L., Price, R., and Rayner, N., 2007, Late-Grenville dextral transcurrent tectonics in the Central Appalachians: Geological Society of America Abstracts with Programs, v. 39, n. 1, p. 49.

Gibson, R. L., Townsend, G. N., Horton, J. J., Kunk, M. J., and Zack, T., 2011, Age of mid-amphibolite facies Alleghanian metamorphism in rocks from the ICDP-USGS Eyreville-B core, Chesapeake Bay impact structure, Virginia: Geological Society of America Abstracts with Programs, v. 43, p. 437.

Glass, J. J., 1935, The pegmatite minerals from near Amelia, Virginia: American Mineralogist, v. 20, n. 11, p. 741–768.

Glover, L., 1989, Tectonics of the Virginia Blue Ridge and Piedmont, *in* Glover, L., III, Evans, N. H., Patterson, J. G., and Brown, W. R., editors, Tectonics of the Virginia Blue Ridge and Piedmont Culpeper to Richmond, Virginia: Washington, D. C., American Geophysical Union, p. 1–52, http://dx.doi.org/10.1029/FT363

Glover, L., III, Speer, J. A., Russell, G. S., and Farrar, S. S., 1983, Ages of regional metamorphism and ductile deformation in the central and southern Appalachians: Lithos, v. 16, n. 3, p. 223–245, http://dx.doi.org/10.1016/0024-4937(83)90026-9

Glover, L., III, Costain, J. K., and Coruh, C., 1995, Chapter 1. Tectonics of the central Appalachian orogen in the vicinity of corridor E-3: With implications for tectonics of the Southern Appalachians, *in* Centennial continent–ocean transect, explanatory pamphlet for transect E- 3, southwestern Pennsylvania to Baltimore Canyon trough: Boulder, Colorado, Geological Society of America, p. 1–49, http://dx.doi.org/10.1130/DNAG-COT-E-3.2

Gundersen, L. C. S., and Gates, A. E., 1995, Mechanical response, chemical variation, and volume change in the Brookneal and Hylas shear zones, Virginia: Journal of Geodynamics, v. 19, n. 3, p. 231–252, http://dx.doi.org/10.1016/0264-3707(94)00016-O

Harlov, D. E., Wirth, R., and Hetherington, C. J., 2011, Fluid-mediated partial alteration in monazite: The role of coupled dissolution-reprecipitation in element redistribution and mass transfer: Contributions to Mineralogy and Petrology, v. 162, n. 2, p. 329–348, http://dx.doi.org/10.1007/s00410-010-0599-7

Harrison, T. M., McKeegan, K. D., and LeFort, P., 1995, Detection of inherited monazite in the Manaslu leucogranite by ^{208}Pb/^{232}Th ion microprobe dating: Crystallization age and tectonic implications: Earth and Planetary Science Letters, v. 133, n. 3–4, p. 271–282, http://dx.doi.org/10.1016/0012-821X(95)00091-P

Harrison, T. M., Grove, M., McKeegan, K. D., Coath, C. D., Lovera, O. M., and Le Fort, P., 1999, Origin and episodic emplacement of the Manaslu intrusive complex, Central Himalaya: Journal of Petrology, v. 40, n. 1, p. 3–19, http://dx.doi.org/10.1093/petroj/40.1.3

Hatcher, R. D., Jr., 2010, The Appalachian orogen: A brief summary: Geological Society of America Memoirs, v. 206, p. 1–19, http://dx.doi.org/10.1130/2010.1206(01)

Heinrich, W., Andrehs, G., and Franz, G., 1997, Monazite-xenotime miscibility gap thermometry. 1. An empirical calibration: Journal of Metamorphic Geology, v. 15, n. 1, p. 3–16, http://dx.doi.org/10.1111/j.1525-1314.1997.t01-1-00052.x

Hellstrom, J. C., Paton, C., Woodhead, J. D., and Hergt, J., 2008, Iolite: software for spatially resolved LA-(quad and MC) ICPMS analysis: Mineralogical Association of Canada Short Course, v. 40, p. 343–348.

Hetherington, C. J., and Harlov, D. E., 2008, Metasomatic thorite and uraninite inclusions in xenotime and monazite from granitic pegmatites, Hidra anorthosite massif, southwestern Norway: Mechanics and fluid chemistry: American Mineralogist, v. 93, n. 5–6, p. 806–820, http://dx.doi.org/10.2138/am.2008.2635

Hetherington, C. J., Jercinovic, M. J., Williams, M. L., and Mahan, K., 2008, Understanding geologic processes with xenotime: Composition, chronology, and a protocol for electron probe microanalysis: Chemical Geology, v. 254, n. 3–4, p. 133–147, http://dx.doi.org/10.1016/j.chemgeo.2008.05.020

Hibbard, J., 2000, Docking Carolina: Mid-Paleozoic accretion in the Southern Appalachians: Geology, v. 28, n. 2, p. 127–130, http://dx.doi.org/10.1130/0091-7613(2000)28<127:DCMAIT>2.0.CO;2

Hibbard, J. P., Stoddard, E. F., Secor, D. T., and Dennis, A. J., 2002, The Carolina Zone: Overview of Neoproterozoic to Early Paleozoic peri-Gondwanan terranes along the eastern flank of the Southern Appalachians: Earth-Science Reviews, v. 57, n. 3–4, p. 299–339, http://dx.doi.org/10.1016/S0012-8252(01)00079-4

Hinchey, A. M., Carr, S. D., and Rayner, N., 2007, Bulk compositional controls on the preservation of age domains within metamorphic monazite: A case study from quartzite and garnet-cordierite-gedrite gneiss of Thor-Odin dome, Monashee complex, Canadian Cordillera: Chemical Geology, v. 240, n. 1–2, p. 85–102, http://dx.doi.org/10.1016/j.chemgeo.2007.02.001

Hoisch, T. D., Wells, M. L., and Grove, M., 2008, Age trends in garnet-hosted monazite inclusions from upper amphibolite facies schist in the northern Grouse Creek Mountains, Utah: Geochimica et Cosmochimica Acta, v. 72, n. 22, 5505–5520, http://dx.doi.org/10.1016/j.gca.2008.08.012

Hokada, T., and Motoyoshi, Y., 2006, Electron microprobe technique for U-Th-Pb and REE chemistry of monazite, and its implications for pre-, peak-, and postmetamorphic events pf the Lützow-Holm Complex and the Napier Complex, East Antarctica: Polar Geoscience, v. 19, p. 118–151.

Holder, R. M., Hacker, B. R., and Kylander-Clark, A. C., 2013, Monazite petrochronology from the UHP Western Gneiss region, Norway: Geological Society of America Abstracts with Programs, v. 45, n. 7, p. 797.

Hollis, J., and Bailey, C., 2012, Kinematic history of brittle deformation and pseudotachylyte in the Hylas fault zone, eastern Piedmont, Virginia. Geological Society of America Abstracts with Programs, v. 44, n. 7, p. 595.

Horton, J. W., Jr., Drake, A. A., Jr., and Rankin, D. W., 1989, Tectonostratigraphic terranes and their Paleozoic boundaries in the central and southern Appalachians, *in* Dallmeyer, R. D., editor, Terranes in the Circum-Atlantic Paleozoic orogens: Geological Society of America Special Papers, v. 230, p. 213–246, http://dx.doi.org/10.1130/SPE230-p213

Horton, J. J., Jr., Berquist, C. J., Marr, J. J., Druhan, R. M., Sacks, P. E., and Butler, J. R., 1993, The Lake Gordon mylonite zone; a link between the Nutbush Creek and Hylas zones of the eastern Piedmont fault system: Geological Society of America Abstracts with Programs, v. 25, n. 4, p. 23.

Horton, J. J., Jr., Aleinikoff, J. N., and Burton, W. C., 1995, Mesoproterozoic and Neoproterozoic terranes in the eastern Piedmont of Virginia, implications of coordinated field studies and U/Pb geochronology: Geological Society of America Abstracts with Programs, v. 27, n. 6, p. 397.

Horton, J. W., Jr., Aleinikoff, J. N., Burton, W. C., Peper, J. D., and Hackley, P. C., 1999, Geologic framework of the Carolina slate belt in southern Virginia; insights from geologic mapping and U/Pb geochronology: Abstracts with Programs, Geological Society of America, v. 31, p. 476.

Horton, J. W., Jr., Daniels, D. L., and Powars, D. S., 2014, Pre-Cretaceous terranes, basins, and faults beneath the Atlantic Coastal Plain; analysis of subsurface samples and borehole data in relation to magnetic and gravity anomalies: Geological Society of America Abstracts with Programs, v. 46, n. 6, p. 59.

Hughes, K. S., Hibbard, J. P., and Miller, B. V., 2013, Relationship between the Ellisville Pluton and Chopawamsic Fault: Establishment of significant Late Ordovician faulting in the Appalachian Piedmont of Virginia: American Journal of Science, v. 313, n. 6, p. 584–612, http://dx.doi.org/10.2475/06.2013.03

Janots, E., Berger, A., Gnos, E., Whitehouse, M., Lewin, E., and Pettke, T., 2012, Constraints on fluid evolution during metamorphism from U–Th–Pb systematics in Alpine hydrothermal monazite: Chemical Geology, v. 326–327, p. 61–71, http://dx.doi.org/10.1016/j.chemgeo.2012.07.014

Jochum, K. P., and Nohl, U., 2008, Reference materials in geochemistry and environmental research and the GeoReM database: Chemical Geology, v. 253, n. 1–2, p. 50–53, http://dx.doi.org/10.1016/j.chemgeo.2008.04.002

Jochum, K. P., Weis, U., Stoll, B., Kuzmin, D., Yang, Q., Raczek, I., Jacob, D. E., Stacke, A., Birbaum, K., Frick, D. A., Gunther, D., and Enzweiler, J., 2011, Determination of Reference Values for NIST SRM 610-617 Glasses Following ISO Guidelines: Geostandards and Geoanalytical Research, v. 35, n. 4, p. 397–429, http://dx.doi.org/10.1111/j.1751-908X.2011.00120.x

Kearns, L. E., 1993, Minerals of the Morefield Pegmatite, Amelia County, Virginia: Rocks and Minerals, v. 68, n. 4, p. 232–242.

——— 1995, Alumino-fluorides from the Morefield Pegmatite, Amelia County, Virginia: Mineralogical Records, v. 26, n. 6, p. 551–556.

Kearns, L. E., and Martin, B. S., 2000, The Morefield Pegmatite, Amelia, Virginia; mineral update: Virginia Minerals, v. 46, n. 2, p. 9–13.

Kempe, U., Lehmann, B., Wolf, D., Rodionov, N., Bombach, K., Schwengfelder, U., and Dietrich, A., 2008, U–Pb SHRIMP geochronology of Th–poor, hydrothermal monazite: An example from the Llallauga tin porphyry deposit, Bolivia: Geochimica et Cosmochimica Acta, v. 72, n. 17, p. 4352–4366, http://dx.doi.org/10.1016/j.gca.2008.05.059

Keppie, J. D., Dostal, J., Murphy, J. B., and Nance, R. D., 1996, Terrane transfer between eastern Laurentia and western Gondwana in the early Paleozoic: Constraints on global reconstructions, *in* Nance, R. D., and Thompson, M. D., editors, Avalonian and Peri-Gondwanan terranes of the Circum–North Atlantic: Geological Society of America Special Papers, v. 304, p. 369–380, http://dx.doi.org/10.1130/0-8137-2304-3.369

Keppler, H., 1993, Influence of fluorine on the enrichment of high field strength trace elements in granitic rocks: Contributions to Mineralogy and Petrology, v. 114, n. 4, p. 479–488. http://dx.doi.org/10.1007/BF00321752

Kish, S. A., and Fullagar, P. D., 1978, Summary of geochronological data for late Paleozoic plutons from high grade metamorphic belts of the eastern Piedmont of North Carolina, South Carolina, and Virginia, *in* Snoke, A. W., editor, Geological investigations of the eastern Piedmont, southern Appalachians (with a field trip guide on the bedrock geology of central South Carolina): US Geological Survey, Carolina Geological Survey Guidebook, p. 41–42.

Koenig, G., 1882, Notes on monazite [Virginia]: Proceedings of the Academy of Natural Sciences of Philadelphia, p. 15–16.

Kohn, M. J., and Vervoort, J. D., 2008, U–Th–Pb dating of monazite by single-collector ICP-MS: Pitfalls and potential: Geochemistry, Geophysics, Geosystems, v. 9, n. 4, p. Q04031, http://dx.doi.org/10.1029/2007GC001899

Krenn, E., and Finger, F., 2010, Unusually Y-rich monazite-(Ce) with 6-14 wt.% Y_2O_3 in a granulite from the Bohemian Massif: Implications for high temperature monazite growth from the monazite-xenotime miscibility gap thermometry: Mineralogical Magazine, v. 74, n. 2, p. 217–225, http://dx.doi.org/10.1180/minmag.2010.074.2.217

Krenn, E., Putz, H. H., Finger, F. F., and Paar, W. H., 2008b, Unusual monazite with high S, Sr, Eu and common Pb contents in ore bearing mylonites from the Schellgaden mining district, Austria: European Geosciences Union, Geophysical Research Abstracts, v. 10, p. EGU2008-a-11796

Krenn, E., Ustaszewski, K., and Finger, F., 2008a, Detrital and newly formed metamorphic monazite in amphibolite-facies metapelites from the Motajica Massif, Bosnia: Chemical Geology, v. 254, n. 3–4, p. 164–174, http://dx.doi.org/10.1016/j.chemgeo.2008.03.012

Krenn, E., Putz, H., Finger, F., and Paar, W. H., 2011, Sulfur-rich monazite with high common Pb in

ore-bearing schists from the Schellgaden mining district (Tauern Window, Eastern Alps: Mineralogy and Petrology, v. 102, p. 51–62, http://dx.doi.org/10.1007/s00710-011-0170-x
Kucha, H., 1980, Continuity in the monazite-huttonite series: Mineralogical Magazine, v. 43, p. 1031–1034, http://dx.doi.org/10.1180/minmag.1980.043.332.12
Kunk, M. J., Horton, J. J., Gibson, R. L., Zack, T., McAleer, R. J., and Townsend, G. N., 2011, Alleghanian thermal history of basement-derived target rocks in the ICDP-USGS Eyreville-B core from the Chesapeake Bay impact structure: Geological Society of America Abstracts with Programs, v. 43, p. 550.
Kylander-Clark, A. C., and Hacker, B. R., 2011, Deciphering the evolution of continental crust; insights through laser ablation split-stream (LASS) petrochronology: Mineralogical Magazine, v. 75, p. 1260.
Kylander-Clark, A. C., Hacker, B. R., and Cottle, J. M., 2013, Laser ablation split stream ICP petrochronology: Chemical Geology, v. 345, p. 99–112, http://dx.doi.org/10.1016/j.chemgeo.2013.02.019
Lambert, C., Groenewald, C., Macey, P., Kisters, A., and Frei, D., 2013, Melt migration along transcurrent shear zones; case study of the Pofadder shear zone and the Skimmelberg pegmatite stockwork: Colloquium of African Geology Abstracts, v. 24, p. 389.
Laughlin, A. W., 1966, Excess radiogenic argon in minerals from the Amelia, Virginia, pegmatites: EOS, Transactions, American Geophysical Union, v. 47, p. 197–198.
——— 1968, A geochronological-geochemical study of the Rutherford and Morefield pegmatites, Amelia, Virginia: EOS, Transactions, American Geophysical Union, v. 49, 761.
——— 1973, Potassium, rubidium and strontium abundances in minerals of the Rutherford and Morefield pegmatites, Amelia, Virginia: Earth and Planetary Science Letters, v. 17, n. 2, p. 375–379, http://dx.doi.org/10.1016/0012-821X(73)90203-3
Lemke, R. W., Jahns, R. H., and Griffitts, W. R., 1952, Amelia district, Virginia, Part 2 of Mica deposits of the southeastern Piedmont: United States Geological Survey Professional Paper, v. 248-B, 139p.
——— 1953, Mica deposits of the southeastern Piedmont, Parts 1-11: United States Geological Survey Professional Paper, v. 248-A, 102 p.
Li, N., Chen, Y., Fletcher, I. R., and Zeng, Q., 2011, Triassic mineralization with Cretaceous overprint in the Dahu AU–Mo deposit, Xiaoqinling gold province: Constraints from SHRIMP monazite U–Th–Pb geochronology: Gondwana Research, v. 20, n. 2–3, p. 543–552, http://dx.doi.org/10.1016/j.gr.2010.12.013
Lobato, L. M., Santos, J. O. S., McNaughton, N. J., Fletcher, I. R., and Noce, C. M., 2007, U–Pb SHRIMP monazite ages of the giant Morro Velho and Cuiabá gold deposits, Rio das Velhas greenstone belt, Quadrilátero Ferrífero, Minas Gerais, Brazil: Ore Geology Reviews, v. 32, n. 3–4, p. 674–680, http://dx.doi.org/10.1016/j.oregeorev.2006.11.007
London, D., 2005, Granitic pegmatites: An assessment of current concepts and directions for the future: Lithos, v. 80, n. 1–4, p. 281–303, http://dx.doi.org/10.1016/j.lithos.2004.02.009
Longerich, H. P., Jackson, S. E., and Günther, D., 1996, Laser ablation inductively coupled plasma mass spectrometric transient signal data acquisition and analyte concentration calculation: Journal of Analytical Atomic Spectroscopy, v. 11, p. 899–904, http://dx.doi.org/10.1039/JA9961100899
Lumpkin, G. R., 1998, Rare-element mineralogy and internal evolution of the Rutherford #2 Pegmatite, Amelia County, Virginia: A classic locality revisited: Canadian Mineralogist, v. 36, n. 2, p. 339–353.
Lupulescu, M. V., Chiarenzelli, J. R., Pullen, A. T., and Price, J. D., 2011, Using pegmatite geochronology to constrain temporal events in the Adirondack Mountains: Geosphere, v. 7, n. 1, p. 23–39, http://dx.doi.org/10.1130/GES00596.1
Lutz, R. D., and Venkatakrishnan, R., 1985, Lineaments in Richmond Triassic basin area, Virginia: A kinematic model: American Association of Petroleum Geologists Bulletin, v. 69, p. 1440.
Mahan, K. H., Williams, M. L., Flowers, R. M., Jercinovic, M. J., Baldwin, J. A., and Bowring, S. A., 2006, Geochronological constraints on the Legs Lake shear zone with implications for regional exhumation of lower continental crust, western Churchill Province, Canadian Shield: Contributions to Mineralogy and Petrology, v. 152, n. 2, p. 223–242, http://dx.doi.org/10.1007/s00410-006-0106-3
Martin, A. J., and Owens, B. E., 2012, Implications of c. 550 Ma crystallization of the Sabot amphibolite protolith in the Goochland Terrane of the central Virginia Piedmont: Geological Society of America Abstracts with Programs, v. 44, n. 7, p. 172.
Martin, A. J., Gehrels, G. E., and DeCelles, P. G., 2007, The tectonic significance of (U,Th)/Pb ages of monazite inclusions in garnet from the Himalaya of central Nepal: Chemical Geology, v. 244, n. 1–2, p. 1–24, http://dx.doi.org/10.1016/j.chemgeo.2007.05.003
Masuda, A., and Nakai, S., 1983, An examination of geochronological utility of electron capture decay of La-138: Geochemical Journal, v. 17, n. 6, p. 313–314, http://dx.doi.org/10.2343/geochemj.17.313
McCauley, A., and Bradley, D. C., 2014, The global age distribution of granitic pegmatites: Canadian Mineralogist, v. 52, n. 2, p. 183–190, http://dx.doi.org/10.3749/canmin.52.2.183
McFarlane, C. R. M., and McCulloch, M. T., 2007, Coupling of *in situ* Sm-Nd systematics and U–Pb dating of monazite and allanite with applications to crustal evolution studies: Chemical Geology, v. 245, n. 1–2, p. 45–60, http://dx.doi.org/10.1016/j.chemgeo.2007.07.020
Michel, J., Cole, K. H., and Moore, W. S., 1982, Uraniferous gorceixite in the South Carolina coastal plain (U.S.A.): Chemical Geology, v. 35, n. 3–4, p. 227–245, http://dx.doi.org/10.1016/0009-2541(82)90003-1
Milton, C., Axelrod, J. M., Carron, M. K., and Stearns MacNeil, F., 1958, Gorceixite from Dale County, Alabama: American Mineralogist, v. 43, n. 7–8, p. 688–694.
Montel, J., Foret, S., Veschambre, M., Nicollet, C., and Provost, A., 1996, Electron microprobe dating of monazite: Chemical Geology, v. 131, n, 1–4, p. 37–53, http://dx.doi.org/10.1016/0009-2541(96)00024-1
Montel, J., Devidal, J., and Avignant, D., 2002, X-ray diffraction study of brabantite-monazite solid solutions: Chemical Geology, v. 191, n. 1–3, p. 89–104, http://dx.doi.org/10.1016/S0009-2541(02)00150-X
Morelli, R. M., Bell, C. C., Creaser, R. A., and Simonetti, A., 2010, Constraints on the genesis of gold mineralization at the Homestake Gold Deposit, Black Hills, South Dakota, from rhenium-osmium

sulfide geochronology: Mineralium Deposita, v. 45, n. 5, p. 461–480, http://dx.doi.org/10.1007/s00126-010-0284-9

Mose, D. G., and Nagel, M. S., 1982, Plutonic events in the Piedmont of Virginia: Southeastern Geology, v. 23, n. 1, p. 25–39

Murata, K. J., Rose, H. J., Jr., and Carron, M. K., 1953, Systematic variation of rare earths in monazite: Geochimica et Cosmochimica Acta, v. 4, n. 6, p. 292–300, http://dx.doi.org/10.1016/0016-7037(53)90058-1

Murphy, J. B., Anderson, A. J., and Archibald, D. A., 1998, Postorogenic alkali feldspar granite and associated pegmatites in West Avalonia: The petrology of the Neoproterozoic Georgeville Pluton, Antigonish Highlands, Nova Scotia: Canadian Journal of Earth Sciences, v. 35, n. 2, p. 110–120, http://dx.doi.org/10.1139/e97-099

Nakai, S. S., Shimizu, H. H., and Masuda, A. A., 1986, A new geochronometer using lanthanum-138: Nature, v. 320, p. 433–435., http://dx.doi.org/10.1038/320433a0

Neuschel, S. K., 1970, Correlation of aeromagnetics and aeroradioactivity with lithology in the Spotsylvania area, Virginia: Geological Society of America Bulletin, v. 81, n. 12, p. 3575–3582, http://dx.doi.org/10.1130/0016-7606(1970)81[3575:COAAAW]2.0.CO;2

Neymark, L. A., Premo, W. R., Mel'nikov, N. N., and Emsbo, P., 2014, Precise determination of δ^{88}Sr in rocks, minerals, and waters by double-spike TIMS: A powerful tool in the study of geological, hydrological and biological processes: Journal of Analytical Atomic Spectrometry, v. 29, n. 1, p. 65–75, http://dx.doi.org/10.1039/C3JA50310K

Ni, Y., Hughes, J. M., and Mariano, A. N., 1995, Crystal chemistry of the monazite and xenotime structures: American Mineralogist, v. 80, n. 1–2, p. 21–26, http://dx.doi.org/10.2138/am-1995-1-203

Okunlola, O., 2013, Tectono-structural framework for metallic mineralization in the basement complex of Nigeria: Colloquium of African Geology Abstracts, 24, 172.

Owens, B. E., Buchwaldt, R., and Shirvell, C. R., 2010, Geochemical and geochronological evidence for Devonian magmatism revealed in the Maidens Gneiss, Goochland Terrane, Virginia: Geological Society of America, Memoirs, v. 206, p. 725–738, http://dx.doi.org/10.1130/2010.1206(28)

Owens, B. E., Buchwaldt, R., and Hancox, C. N., 2015, Further evidence for Devonian magmatism revealed in the Maidens Gneiss, Goochland Terrane, Virginia: Geological Society of America Abstracts with Programs, Paper No. 131–12.

Papoutsa, A. D., and Pe-Piper, G., 2013, The relationship between REE-Y-Nb-Th minerals and the evolution of an A-type granite, Wentworth Pluton, Nova Scotia: American Mineralogist, v. 98, n. 2–3, p. 444–462, http://dx.doi.org/10.2138/am.2013.3972

Parrish, R. R., 1990, U–Pb dating of monazite and its application to geological problems: Canadian Journal of Earth Sciences, v. 27, n. 11, p. 1431–1450, http://dx.doi.org/10.1139/e90-152

Pavlides, L., Stern, T. W., Arth, J. G., Muth, K. G., and Newell, M. F., 1982, Middle and upper Paleozoic granitic rocks in the Piedmont near Fredericksburg, Virginia; geochronology: United States Geological Survey Professional Paper, p. B1-B9.

Pavlides, L., Arth, J. G., Sutter, J. F., Stern, T. W., and Cortesini, H., 1994, Early Paleozoic alkalic and calc-alalkalic plutonism and associated contact metamorphism, central Virginia piedmont: United States Geological Survey Professional Paper, v. 1529, 147 p.

Pegau, A., 1932, Pegmatite deposits of Virginia: Bulletin of the Virginia Geological Survey, 123 p.

Penfield, S. L., 1882, On the occurrence and composition of some American varieties of monazite: American Journal of Science, Series 3, v. 24, n. 142, p. 250–254, http://dx.doi.org/10.2475/ajs.s3-24.142.250

Peterman, E. M., Hacker, B. R., Grove, M., Gehrels, G. E., and Mattinson, J. M., 2006, A multimethod approach to improving monazite geochronology: Eos, Transactions American Geophysical Union, Fall Meeting 2006, abstract #V21A-0551, 2006AGUFM.V21A0551P

Peterman, E. M., Mattinson, J. M., and Hacker, B. R., 2012, Multi-step TIMS and CA-TIMS monazite U/Pb geochronology: Chemical Geology, v. 312–313, p. 58–73, http://dx.doi.org/10.1016/j.chemgeo.2012.04.006

Petrik, I., Kubis, M., Konecny, P., Broska, I., and Malachovsky, P., 2011, Rare phosphates from the Surovec topaz-Li-mica microgranite, Gemeric Unit, Western Carpathians, Slovak Republic: Role of F/H_2O of the melt: Canadian Mineralogist, v. 49, n. 2, p. 521–540, http://dx.doi.org/10.3749/canmin.49.2.521

Pulver, M. H., Coleman, M. E., Byrne, T., Wintsch, R. P., Kunk, M. J., Boyd, J. L., and Dunnigan, J., 1997, Structure and chronology of a section of the Bronson Hill Terrane; significance for late Paleozoic to early Mesozoic exhumation in south-central New England: Geological Society of America Abstracts with Programs, v. 29, p. 231.

Qureshi, R. H., Jenkins, D. A., Davies, R. I., and Rees, J. A., 1969, Application of microprobe analysis to the study of phosphorus in soils: Nature, v. 221, p. 1142–1143, http://dx.doi.org/10.1038/2211142a0

Rankin, D. W., Drake, A. A., Jr., Glover, L., III, Goldsmith, R., Hall, L. M., Murray, D. P., Ratcliffe, N. M., Read, J. F., Secor, D. T., Jr., and Stanley, R. S., 1989, Pre-orogenic terranes, *in* Hatcher, R. D., Jr., Thomas, W. A., and Viele, G. W., editors, The Appalachian-Ouachita orogen in the United States: Boulder, Colorado, Geological Society of America, The Geology of North America, v. F-2, p. 7–100, http://dx.doi.org/10.1130/DNAG-GNA-F2.7

Rasmussen, B., 1996, Early-diagenetic REE-phosphate minerals (florencite, gorceixite, crandallite, and xenotime) in marine sandstones: A major sink for oceanic phosphorus: American Journal of Science, v. 296, n. 6, p. 601–632, http://dx.doi.org/10.2475/ajs.296.6.601

Reno, B. L., Piccoli, P. M., Brown, M., and Trouw, R. A. J., 2012, *In situ* monazite (U-Th)-Pb ages from the Southern Brasília Belt, Brazil: Constraints on the high temperature retrograde evolution of HP granulites: Journal of Metamorphic Geology, v. 30, n. 1, p. 81–112, http://dx.doi.org/10.1111/j.1525-1314.2011.00957.x

Robinson, P., Tucker, R. D., Berry, H. N., Peterson, V. L., and Thompson, P. J., 2007, U-Pb geochronology of

Late Devonian through Late Pennsylvanian deformation and high-grade metamorphism in central Massachusetts and adjacent New Hampshire, with speculations about broader tectonic settings: Geological Society of America Abstracts with Programs, v. 39, p. 68.

Rojkovic, I., Konecny, P., Novotny, L., Puskelova, L., and Stresko, V., 1999, Quartz-apatite-REE vein mineralization in early Paleozoic rocks of the Gemeric Superunit, Slovakia: Geologica Carpathica, v. 50, p. 215–227.

Rollinson, G. K., Pirrie, D. D., Power, M. R., Cundy, A. A., and Camm, G. S., 2007, Geochemical and mineralogical record of historical mining, Hayle Estuary, Cornwall, United Kingdom: Proceedings of the Ussher Society, v. 11, p. 326–337.

Sacks, P. E., 1999, Geologic Overview of the Eastern Appalachian Piedmont along Lake Gaston, North Carolina and Virginia, *in* Saks, P. E., editor, Geology of the Fall Zone Region along the North Carolina – Virginia State Line: Guidebook for the 1999 Meeting of the Carolina Geological Society, Emporia, Virginia, p. 1–15.

Sallet, R., Price, J. D., Babinski, M., Moritz, R., Souza, Z. S., and Chiaradia, M., 2015, Experimental anatexis, fluorine geochemistry and lead-isotope constraints on granite petrogenesis in the Seridó Belt, Borborema Province, northeastern Brazil: Chemical Geology, v. 400, p. 122–148, http://dx.doi.org/10.1016/j.chemgeo.2015.02.011

Seydoux-Guillaume, A., Paquette, J., Wiedenbeck, M., Montel, J., and Heinrich, W., 2002, Experimental resetting of the U-Th-Pb systems in monazite: Chemical Geology, v. 191, n. 1–3, p. 165–181, http://dx.doi.org/10.1016/S0009-2541(02)00155-9

Seydoux-Guillaume, A., Montel, J., Bingen, B., Bosse, V., de Parseval, P., Paquette, J., Janots, E., and Wirth, R., 2012, Low-temperature alteration of monazite: Fluid mediated coupled dissolution-precipitation, irradiation damage, and disturbance of the U-Pb and Th-Pb chronometers: Chemical Geology, v. 330–331, p. 140–158, http://dx.doi.org/10.1016/j.chemgeo.2012.07.031

Shannon, R. D., 1976, Systematic studies of interatomic distances in oxides: London, John Wiley and Sons, p. 403–431.

Sheard, E. R., Williams-Jones, A. E., Heiligmann, M., Pederson, C., and Trueman, D. L., 2012, Controls on the concentration of zirconium, niobium, and the rare earth elements in the Thor Lake rare metal deposit, Northwest Territories, Canada: Economic Geology, v. 107, n. 1, p. 81–104, http://dx.doi.org/10.2113/econgeo.107.1.81

Sinha, A. K., Thomas, W. A., Hatcher, R. D., Jr., and Harrison, T. M., 2012, Geodynamic evolution of the central Appalachian Orogen: Geochronology and compositional diversity of the magmatism from Ordovician through Devonian: American Journal of Science, v. 312, n. 8, p. 907–966, http://dx.doi.org/10.2475/08.2012.03

Sinkankas, J., 1968, Classical mineral occurrences: I. Geology and mineralogy of the Rutherford pegmatites, Amelia, Virginia: American Mineralogist, v. 53, n. 3–4, p. 373–405.

Smerekanicz, J. R., and Dudas, F. O., 1999, Reconnaissance fluid inclusion study of the Morefield Pegmatite, Amelia County, Virginia: American Mineralogist, v. 84, n. 5–6, p. 746–753, http://dx.doi.org/10.2138/am-1999-5-606

Spear, F. S., and Pyle, J. M., 2010, Theoretical modeling of monazite growth in a low Ca metapelite: Chemical Geology, v. 273, n. 1–2, p. 111–119, http://dx.doi.org/10.1016/j.chemgeo.2010.02.016

Spears, D. B., Owens, B. E., and Bailey, C. M., 2004, The Goochland-Chopawamsic Terrane boundary, central Virginia Piedmont: United States Geological Survey Circular 1264, p. 223–245, http://pubs.usgs.gov/circ/2004/1264/html/trip7/index.html

Staatz, M. H., Sharp, B. J., and Hetland, D. L., 1979, Geology and mineral resources of the Lemhi Pass thorium district, Idaho and Montana: United States Geological Survey Professional Paper, v. 1049–A, p. 1–90, http://pubs.er.usgs.gov/publication/pp1049A

Stevens, L. M., and Baldwin, J. A., 2013, Phase equilibria, garnet REE geochemistry, and LASS petrochronology; constraints on the P-T-t history of the Priest River Complex, northern Idaho: Geological Society of America Abstracts with Programs, v. 45, n. 7, p. 880.

Sun, S-s., and McDonough, W. F., 1989, Chemical and isotopic systematic of ocean basalts: Implications for mantle composition and processes: Geological Society, London, Special Publications, v. 42, p. 313–345, http://dx.doi.org/10.1144/GSL.SP.1989.042.01.19

Suzuki, K., Adachi, M., and Kajizuka, I., 1994, Th, U and Pb analytical data of monazites used in the paper, electron microprobe observations of Pb diffusion in metamorphosed detrital monazite. Journal of Earth Planetary Sciences, Nagoya University, v. 41, p. 75–81.

Sweatman, T. R., ms, 1961, The mineralogy and chemistry of the phosphate minerals in some soils: Adelaide, Australia, University of Adelaide, M.S. thesis, Australia, 133 p.

Taber, S., 1913, Geology of the gold belt in the James River basin, Virginia: Virginia Geological Survey Bulletin, 847 p.

Taylor, M., Smith, R. W., and Ahler, B. A., 1984, Gorceixite in topaz greisen assemblages Silver mine area, Missouri: American Mineralogist, v. 69, n, 9–10, p. 984–986.

Tilton, G. R., and Nicolaysen, L. O., 1957, The use of monazites for age determination: Geochimica et Cosmochimica Acta, v. 11, n. 1–2, p. 28–40, http://dx.doi.org/10.1016/0016-7037(57)90003-0

Triantafyllidis, S., Pe-Piper, G., MacKay, R., Piper, D. J. W., and Strathdee, G., 2010, Monazite as a provenance indicator for the Lower Cretaceous reservoir sandstones, Scotian Basin: Geological Survey of Canada Open File, v. 6732, 452 p., http://dx.doi.org/10.4095/287317

Tropper, P., Manning, C. E., and Harlov, D. E., 2013, Experimental determination of $CePO_4$ and YPO_4 solubilities in H_2O-NaF at 800 °C and 1 Gpa: Implications for rare earth element transport in high-grade metamorphic fluids: Geofluids, v. 13, n. 3, p. 372–380, http://dx.doi.org/10.1111/gfl.12031

Upadhyay, D., and Pruseth, K. L., 2012, Fluid-induced dissolution breakdown of monazite from Tso Morari

Complex, NW Himalayas: Evidence for immobility of trace elements: Contributions to Mineralogy and Petrology, v. 164, n. 2, p. 303–316, http://dx.doi.org/10.1007/s00410-012-0739-3

van Hees, E. H., Sirbescu, M-L.C., Shelton, K. L., and Pressacco, R., 2002, Supergene phosphate enrichment in carbonatite-derived eluvial sediments; Agrium phosphate mine, Kapuskasing, Ontario, Canada: Geological Society of America Abstracts with Programs, v. 34, p. 312.

Venkatakrishnan, R., 1987, Mesozoic brittle reactivation of the Hylas fault zone; developmental model for the Richmond Basin, Virginia: Geological Society of America Abstracts with Programs, v. 19, n. 2, p. 134.

Venkatakrishnan, R., and Watkins, A., 1988, Mesoscopic analysis of brittle deformation zones and fault rocks; Mesozoic extensional reactivation of the late Paleozoic Hylas fault zone, Virginia: Proceedings of the International Conference on Basement Tectonics, p. 834.

Viana, R. R., Mänttäri, I., Kunst, H., and Jordt-Evangelista, H., 2003, Age of pegmatites from eastern Brazil and implications of mica intergrowths on cooling rates and age calculations: Journal of South American Earth Sciences, v. 16, n. 6, p. 493–501, http://dx.doi.org/10.1016/S0895-9811(03)00105-6

Virginia Department of Mines Report (VDMR), 2003, Digital Representation of the 1993 Geologic Map of Virginia, Virginia Department of Mines, Minerals, and Energy Publication 174, Model Number: 1352.

Walsh, G. J., Aleinikoff, J. N., and Wintsch, R. P., 2007a, Origin of the Lyme Dome and implications for the timing of multiple Alleghanian deformational and intrusive events in southern Connecticut: American Journal of Science, v. 307, n. 1, p. 168–215, http://dx.doi.org/10.2475/06.2007.06

Walsh, G. J., Aleinikoff, J. N., and Wintsch, R. P., 2007b, Timing of Alleghanian orogenesis and dome formation in southern Connecticut. Geological Society of America Abstracts with Programs, v. 39, p. 80.

Watt, G. R., 1995, High-thorium monazite-(Ce) formed during disequilibrium melting of metapelites under granulite-facies conditions: Mineralogical Magazine, v. 59, p. 735–743, http://dx.doi.org/10.1180/minmag.1995.059.397.14

Wawrzenitz, N., Krohe, A., Rhede, D., and Romer, R. L., 2012, Dating rock deformation with monazite: The impact of dissolution precipitation creep: Lithos, v. 134–135, p. 52–74, http://dx.doi.org/10.1016/j.lithos.2011.11.025

Weems, R. E., ms, 1974, Geology of the Hanover Academy and Ashland quadrangles, Virginia: Blacksburg, Virginia, Virginia Polytechnic Institute and State University, Blacksburg, M. S. Thesis, 100 p

Wilson, J. R., ms, 2001, U/Pb Ages of plutons from the Central Appalachians and GIS-based assessment of plutons with comments on their regional tectonic significance: Blacksburg, Virginia, Virginia Polytechnic Institute and State University, M.S. Thesis, 109 p.

Wortman, G. L., Samson, S. D., and Hibbard, J. P., 1998, Precise timing constraints on the kinematic development of the Hyco shear zone: Implications for the central Piedmont shear zone, Southern Appalachian Orogen: American Journal of Science, v. 298, n. 2, p. 108–130, http://dx.doi.org/10.2475/ajs.298.2.108

Wright, J. E., Sinha, A. K., and Glover, L., III, 1975, Age of zircons from the Petersburg Granite, Virginia: With comments on belts of plutons in the Piedmont: American Journal of Science, v. 275, n. 7, p. 848–856, http://dx.doi.org/10.2475/ajs.275.7.848

Xu, P., Guan, H., Sun, M., and Malps, J., 2000, Methodology of trace element in situ analyses using laser ablation inductively coupled plasma mass spectrometry: Acta Petrologica Sinica, v. 16, p. 291–304.

Young, E., Myers, A., Munson, E., and Conklin, N., 1969, Mineralogy and geochemistry of fluorapatite from Cerro de Mercado, Durango, Mexico: US Geological Survey Professional Paper, v. 650D, p. D84–D93.

Zhou, X., Zhao, G., Wei, C., Geng, Y., and Sun, M., 2008, EPMA U-Th-Pb monazite and SHRIMP U-Pb zircon geochronology of high-pressure pelitic granulites in the Jiaobei Massif of the North China Craton: American Journal of Science, v. 308, n. 3, p. 328–350, http://dx.doi.org/10.2475/03.2008.06

Zhu, X. K., and O'Nions, R. K., 1999, Zonation of monazite in metamorphic rocks and its implications for high temperature thermochronology: A case study from the Lewisian terrain: Earth and Planetary Science Letters, v. 171, n. 2, p. 209–220, http://dx.doi.org/10.1016/S0012-821X(99)00146-6

View publication stats